



Deposited via The University of Sheffield.

White Rose Research Online URL for this paper:

<https://eprints.whiterose.ac.uk/id/eprint/220292/>

Version: Accepted Version

Article:

Adedeji-Olulana, A.F., Wacnik, K., Lafage, L. et al. (2024) Two codependent routes lead to high-level MRSA. *Science*, 386 (6721). pp. 573-580. ISSN: 0036-8075

<https://doi.org/10.1126/science.adn1369>

© 2024 The Authors. Except as otherwise noted, this author-accepted version of a journal article published in *Science* is made available via the University of Sheffield Research Publications and Copyright Policy under the terms of the Creative Commons Attribution 4.0 International License (CC-BY 4.0), which permits unrestricted use, distribution and reproduction in any medium, provided the original work is properly cited. To view a copy of this licence, visit <http://creativecommons.org/licenses/by/4.0/>

Reuse

This article is distributed under the terms of the Creative Commons Attribution (CC BY) licence. This licence allows you to distribute, remix, tweak, and build upon the work, even commercially, as long as you credit the authors for the original work. More information and the full terms of the licence here:

<https://creativecommons.org/licenses/>

Takedown

If you consider content in White Rose Research Online to be in breach of UK law, please notify us by emailing eprints@whiterose.ac.uk including the URL of the record and the reason for the withdrawal request.

Two co-dependent routes lead to high-level MRSA

Abimbola Feyisara Adedeji-Olulana^{1†}, Katarzyna Wacnik^{2,3,†}, Lucia Lafage^{2,3}, Laia Pasquina-Lemonche^{1,3}, Mariana Tinajero-Trejo^{2,3}, Joshua A. F. Sutton^{2,3}, Bohdan Bilyk^{2,3}, Sophie E. Irving^{2,3}, Callum J. Portman Ross^{2,3}, Oliver J. Meacock¹, Sam A. Randerson¹, Ewan Beattie¹, David S. Owen^{2‡}, James Florence^{2,3}, William M. Durham¹, David P. Hornby^{2,3}, Rebecca M. Corrigan^{2,3,4}, Jeffrey Green^{2,3}, Jamie K. Hobbs^{1,*}, Simon J. Foster^{2,3,*}

¹ Department of Physics and Astronomy, University of Sheffield, Sheffield, UK.

² School of Biosciences, University of Sheffield, Sheffield, UK.

³ The Florey Institute, University of Sheffield, Sheffield, UK.

⁴ School of Medicine, University College Dublin, Dublin, Ireland.

[†] These authors contributed equally to this work.

[‡] Present address. Department of Biosciences and Chemistry, Sheffield Hallam University, UK.

* Corresponding author. Email : jamie.hobbs@sheffield.ac.uk; s.foster@sheffield.ac.uk.

One Sentence Summary

High-level resistance in MRSA requires two pathways that reveal a novel cell division mode.

Abstract

Methicillin resistant *S. aureus* (MRSA) is of major clinical concern, in which acquisition of *mecA*, encoding the cell wall peptidoglycan biosynthesis component Penicillin Binding Protein 2a (PBP2a), confers resistance to β -lactam antibiotics. In the presence of antibiotics we show that MRSA adopts an alternative cell division mode, with altered peptidoglycan architecture at the division septum. PBP2a can replace the transpeptidase activity of the endogenous and essential PBP2, but not that of PBP1, which is responsible for the distinctive native septal peptidoglycan architecture. Successful division without PBP1 activity, requires the alternative division mode and is enabled by several possible chromosomal, potentiator (*pot*) mutations. MRSA resensitizing agents differentially interfere with the two co-dependent mechanisms required for high-level antibiotic resistance, providing opportunities for new interventions.

Introduction

Antibiotics are at the heart of modern medicine, but their efficacy is increasingly challenged by the spread of antimicrobial resistance (AMR) (1). MRSA is a so-called AMR “superbug”, that causes over 120,000 deaths per annum (2). Methicillin was introduced to circumvent clinical β -lactamase-mediated resistance, but soon became compromised due to the spread of MRSA (3). Resistance in MRSA is primarily based on the acquisition of the *mecA* gene encoding a novel PBP, named PBP2a, characterised by its low affinity for a broad range of β -lactams (3, 4). The *mecA* gene is carried on a mobile genetic element, the staphylococcal cassette chromosome (*SCCmec*) (3). *SCCmec* elements are classified into several types, including I, II, and III, which are primarily hospital-associated clones, and types IV and V often identified in community-associated MRSA (3).

42 PBPs are enzymes that carry out the final stages of assembly of bacterial cell wall
43 peptidoglycan (PG). Cell wall PG is essential for viability of most bacteria and forms a single
44 macromolecule around the cell (the sacculus), made of glycan strands and cross-linked via
45 peptide side-chains (5). High resolution Atomic Force Microscopy (AFM) has recently
46 revealed *S. aureus* PG to be a porous, heterogeneous hydrogel (6). Its mature surface is an
47 open, disordered mesh with pores that penetrate deep into the wall, whereas the inner surface,
48 where PG is synthesised, is a much denser mesh (6). Another feature of the PG is an outer
49 architecture of concentric rings consisting of long glycan strands that is revealed upon cell
50 scission and is characteristic of the newly exposed septum (6).

51 *S. aureus* has four endogenous PBPs of which only PBP1 and 2 are essential for PG synthesis,
52 being able to carry out all the transpeptidase (linking side-chains) functions necessary for cell
53 growth and division (7, 8, 9). PBP1 has multiple roles in cell division, by acting as a
54 coordinator, through interactions with PG and divisome protein partners, and by providing the
55 transpeptidase activity that is thought to be required for the characteristic ring architecture in
56 septal PG (6, 7, 8).

57 PBP2a is a non-native enzyme in MRSA, acquired from an environmental source, so how it
58 facilitates high-level antibiotic resistance by replacing the transpeptidase activity of
59 endogenous PBPs is intriguing. PBP2a requires the transglycosylase activity of PBP2 to
60 mediate resistance and the two proteins interact, thus demonstrating their functional
61 cooperativity (10). PBP2a can maintain transpeptidase activity with a closed active site
62 conformation, thus resisting β -lactam binding while interaction with a second PG substrate
63 molecule at an allosteric site leads to a conformational change that opens the active site for
64 catalysis (11).

65 An interesting feature of many clinical MRSA isolates is that they exhibit heterogeneous
66 resistance, whereby only a very small proportion ($<10^{-4}$) of the population are high-level
67 resistant ($>50 \mu\text{g ml}^{-1}$ methicillin) (12). Antibiotics can induce the conversion of the population
68 to homogeneous high-level resistance, that does not revert in the absence of antibiotics.
69 Chromosomal mutations that lead to the conversion to homogeneous resistance, mostly map to
70 genes responsible for the regulation of aspects of cellular physiology and not PBP2a function
71 directly (13). We have named these genes “potentiators” (*pot*), to differentiate them from
72 auxiliary genes (*aux*), in which mutation leads to decreased resistance (13). We have recently
73 carried out a directed evolution study that provides matched strains enabling the exploration of
74 MRSA resistance mechanisms (14). Development of high-level MRSA is a two-step process
75 whereby the presence of *mecA* is essential but in itself only results in a modest increase in
76 minimum inhibitory concentration (MIC) (low-level MRSA). Acquisition of missense
77 mutations in genes encoding RNA polymerase subunits (*rpoB* or *rpoC*), so-called *rpo**
78 mutations, potentiate a step-change in resistance levels (high-level MRSA), both in the clinical
79 environment and under laboratory conditions (13, 14).

80 Cell wall architecture of MRSA

81 AFM was used to analyse the nanoscale, PG architecture, where in all cases at least 20
82 individual sacculi (i.e. purified cell wall fragments) were examined (see Materials and
83 Methods). AFM analysis (Fig. 1A-B; and fig. S1A-B and S2A-B) showed that low-level
84 resistant MRSA (SH1000 *mecA*⁺ (hereafter designated *mecA*⁺); MIC $2 \mu\text{g ml}^{-1}$), in the absence
85 of methicillin, resembled its sensitive parent (SH1000; MIC $0.25 \mu\text{g ml}^{-1}$). In both cases, the
86 inner surface of the cell wall in all areas consisted of a dense mesh of PG, the outer surface of
87 the septum, newly exposed after division, exhibited the characteristic septal PG concentric-
88 ring architecture, and the PG at the outer surface of the cell, away from the most recent site of

89 division, consisted of an open mesh structure (6) (Fig. 1A-B; and fig. S1A-B, S2A-B). We
90 quantified the orientation of individual glycan strands for strains SH1000 and *mecA*⁺ in the
91 absence of antibiotic using a custom-made automated image analysis. This revealed that in
92 both cases the outer surface of the septum exhibited a prominent peak in the circumferential
93 direction that is consistent with the concentric-ring architecture (Fig. 1Aiii, Biii). However, no
94 PG concentric rings were apparent at the outer surface of the septum of *mecA*⁺ in the presence
95 of 1.5 µg ml⁻¹ methicillin (sub-MIC for *mecA*⁺). Rather, the outer surface of the septum
96 appeared as a dense mesh structure (Fig. 1Di-iii), while the inner surface displayed a large
97 proportion of long glycan strands that were oriented near the septal centre (fig. S1Dii, see the
98 long orange-brown coloured-fibres in fig. S1Diii). Furthermore, the cell wall was thinner after
99 treatment with methicillin (fig. S1F). Under the same conditions (1.5 µg ml⁻¹ methicillin), the
100 parental strain, SH1000, died and cell wall spanning holes were apparent (15) (fig. S2F-H). The
101 cell wall architecture of the high-level MRSA strain (SH1000 *mecA*⁺ *rpoB*^{*} (hereafter
102 designated *mecA*⁺ *rpoB*^{*}); MIC ≥256 µg ml⁻¹), which possessed both *mecA* and the *pot*
103 mutation, *rpoB*^{*} coding for a variant of the RNA polymerase β subunit RpoB(H929Q) (14),
104 resembled that of the parental strain (*mecA*⁺) in the absence of antibiotics (Fig. 1C; and fig.
105 S1C and fig. S2C). When treated with 25 µg ml⁻¹ methicillin (sub-MIC for this strain but
106 sufficient to kill both SH1000 and *mecA*⁺) the inner surface of the cell wall maintained a dense
107 network of PG mesh, without the appearance of perforating holes (fig. S1Eii). However, in the
108 large majority of cases, the septa were thickened with a distinct protuberance, or lump, at the
109 centre (fig. S1Ei). Importantly, although *mecA*⁺ *rpoB*^{*} was able to grow and divide in the
110 presence of methicillin, there was a total absence of the PG concentric-ring structure on the
111 outer surface of newly divided cells (Fig. 1E). Septal PG concentric rings are a defining feature
112 of PG architecture in several gram-positive bacteria (6, 16). Instead of PG concentric rings, the
113 outer surface of septa obtained from methicillin-treated *mecA*⁺ *rpoB*^{*} consisted of a disordered,
114 dense mesh with small pore size (Fig. 1E). As in the absence of antibiotics, the outer surface
115 of the rest of the cell periphery appeared as a more open mesh with larger pore size (fig. S2E
116 and S2I). This open mesh structure is derived from the dense mesh rather than from the
117 concentric ring structure, which remodels as cells divide in different planes during subsequent
118 division rounds (16). An interpretative diagram illustrating these observations is shown in Fig.
119 1F.

120 We then used the clinical, high-level, MRSA strain COL (SCC*mec* Type I), which possesses
121 both the *mecA* gene and produces a variant RpoB(A798V, S875L) (14) (MIC ≥256 µg ml⁻¹) to
122 determine whether the resistance-associated PG architectural changes described above
123 (absence of septal PG concentric rings, retention of PG dense mesh without perforating holes)
124 are a common feature of MRSA cells under antibiotic stress. The COL cells were smaller than
125 SH1000 (average cell volume 0.69 ± 0.14 vs 1.22 ± 0.31 µm³) as were the cells of *mecA*⁺ *rpoB*^{*}
126 (average cell volume 0.60 ± 0.20 µm³, fig. S4D). Without antibiotics, COL displayed septal
127 PG concentric rings (fig. S3A), whereas in the presence of 25 µg ml⁻¹ methicillin (sub-MIC),
128 the septal PG of COL exhibited no concentric rings, but rather a disordered, dense mesh, at the
129 septal outer surface (fig. S3G). Treatment of *mecA*⁺, *mecA*⁺ *rpoB*^{*} and COL with sub-MIC
130 concentrations of antibiotics (1.5, 25, and 25 µg ml⁻¹, respectively) led to high levels of PG
131 synthesis at the septum (as observed by ADA-DA incorporation), an increase in cell volume
132 and septal abnormalities observed by fluorescence microscopy and transmission electron
133 microscopy (TEM) (fig. S4).

134 To demonstrate the wider applicability of our findings we then analyzed representatives of
135 different MRSA lineages and SCC*mec* types (SCC*mec* II (Mu50, MRSA252), III (TW20) and
136 IV (USA300, EMRSA15)) (3, 17-20). All strains had methicillin MICs of >256 µg ml⁻¹ apart
137 from EMRSA15 and USA300 (MIC 64 and 1-2 µg ml⁻¹, respectively) (Table S1). High-level

138 MRSA derivatives ($\text{MIC} > 256 \mu\text{g ml}^{-1}$), of the latter two strains, designated USA300 (HL) and
139 EMRSA15 (HL), were selected by directed evolution on oxacillin gradient plates (see
140 Materials and Methods).

141 AFM analysis of the clinical strains and high-level resistant derivatives was carried out in the
142 absence and presence of $25 \mu\text{g ml}^{-1}$ methicillin (sub-MIC; fig. S3). All untreated strains had
143 septal PG concentric rings at the outer face of the septum (fig. S3). In the presence of $25 \mu\text{g}$
144 ml^{-1} methicillin (sub-MIC), the septal PG of COL, EMRSA15 (HL) and USA300 (HL) had a
145 disordered, dense mesh, at the septal outer surface but Mu50, MRSA252 and TW20 had
146 occasional (10 - 30% of septa) residual PG orientation. Growth of Mu50, MRSA252, and
147 TW20 in $50 \mu\text{g ml}^{-1}$ methicillin (sub-MIC) gave rise to disordered mesh at the septal outer
148 surface (fig. S3). Thus, similar adaptations in septal PG architecture in response to antibiotic
149 challenge are conserved across MRSA strains (Fig. 1F).

150 Thus, even though PBP2a, in MRSA backgrounds permits growth and division in the presence
151 of antibiotics, it leads to profound changes to cell wall architecture. This raises the questions
152 as to how PBP2a complements the loss of both essential PBP1 and PBP2 transpeptidase
153 activities, and also how high-level MRSA is able to divide?

154 **Mode of cell division underpins high-level MRSA**

155 We have recently suggested that the *S. aureus* septal PG concentric rings are due to PBP1
156 transpeptidase activity (8). Methicillin sensitive *S. aureus* (MSSA) specifically lacking PBP1
157 transpeptidase activity is not viable and exhibits aberrant septa (8). However, a high-level
158 MRSA strain with the same site-directed inactivation of PBP1 transpeptidase activity can grow
159 (8), suggesting that PBP2a complements the lack of PBP1 activity, but perhaps without the
160 ability to construct the septal PG concentric-ring structures. We therefore constructed a set of
161 otherwise isogenic strains where, in the absence of the inducer IPTG, only PBP1 without
162 transpeptidase activity (PBP1*) was expressed (Fig. 2A; and fig. S5A and B). Wholly
163 unexpectedly, the presence of PBP2a in this background SH1000 *P_{spac}-pbp1 pbp1* mecA⁺*
164 (hereafter designated *pbp1* mecA⁺*) did not complement the loss of PBP1 transpeptidase
165 activity, demonstrating that PBP2a cannot substitute for the essential transpeptidase function
166 of PBP1 (Fig. 2B). Conversely, a single point mutation in *rpoB* (resulting in amino acid
167 replacement H929Q; *rpoB**), that is required for MRSA with high-level resistance (14), was
168 able to entirely restore the ability of PBP1* to grow in the absence of PBP2a (Fig. 2B; and fig.
169 S5C and D). Growth of *P_{spac}-pbp1 pbp1* rpoB** (hereafter designated *pbp1* rpoB**) without
170 IPTG was associated with septal abnormalities, an increase in cell volume, and alterations to
171 PG synthesis (Fig. 2C and D; and fig. S5E-F and S6A), similar to high-level MRSA grown in
172 the presence of antibiotics (fig. S4B).

173 AFM analysis of the PG architecture of *pbp1* rpoB** with IPTG (PBP1 transpeptidase activity
174 present) revealed open mesh on outer surfaces and septal PG concentric rings as expected for
175 a wild type strain (Fig. 2E (+IPTG); Fig. S6B to D). However, growth without IPTG (no PBP1
176 transpeptidase activity) led to the concentric rings at the septal surface being replaced by a
177 disordered, dense mesh with random glycan strand orientation (Fig. 2E (-IPTG); and fig. S6E
178 to G). Although *rpoB** complemented the absence of PBP1 transpeptidase activity, neither
179 *rpoB** nor PBP2a, or both combined, could rescue cells lacking the PBP1 protein (fig. S7),
180 consistent with the physical presence of PBP1 being necessary for cell division complex
181 assembly. Therefore, the septal PG ring architecture associated with conventional cell division
182 requires the essential transpeptidase activity of PBP1, but *S. aureus* can adopt an alternative
183 division mode facilitated by *rpoB** when PBP1 transpeptidase activity is lost (either by
184 mutation or antibiotic addition; Fig. 1F). This fundamentally different mode of cell division,

185 which lacks the canonical septal PG concentric-ring architecture, is exploited in high-level
186 MRSA, where *rpoB** in combination with *mecA* allows division in the presence of antibiotics.

187 **Dual mechanisms for high-level MRSA**

188 High-level MRSA requires two factors; the presence of PBP2a and a potentiator (*pot*) mutation
189 (as provided by *rpoB**) (13, 14). For high-level MRSA to grow and divide in the presence of
190 β -lactam antibiotics, the essentiality of PBP1 and PBP2 transpeptidase activities must be
191 circumvented or enzymatically complemented. Previous studies report that in strain COL the
192 transpeptidase activity of PBP2 can be complemented by the presence of PBP2a (21, 22).
193 However, growth of a COL derivative lacking PBP2 protein is impaired and does not exhibit
194 antibiotic resistance (22). This is because PBP2 transglycosylase activity is required to act
195 cooperatively with PBP2a (22). COL also harbours potentiator *rpoB** mutations (A798V,
196 S875L) required for high-level resistance (14). To determine whether there are two co-
197 dependent mechanisms that in combination lead to high-level MRSA we investigated the effect
198 of *pbp2* mutations. As expected from previous reports (21, 22) PBP2 is essential and PBP2a
199 and/or *rpoB** (H929Q) could not compensate for the loss of PBP2 protein in terms of plating
200 efficiency and growth (fig. S8A-C). When PBP2 was depleted, with or without the presence of
201 PBP2a, *S. aureus* stopped dividing, exhibiting decreased septal PG incorporation and altered
202 septal morphology (fig. S9). Loss of PBP2 also led to a decrease in cell size (fig. S9H).
203 Depletion of PBP2 in *rpoB** or *mecA⁺ rpoB** led to lower growth, decreased septal PG
204 incorporation, altered septal morphology, and death (fig. S9C, D, and G). We could not create
205 PBP2* (transpeptidase mutant) strains in either the parental SH1000 or *rpoB** backgrounds,
206 indicating its essentiality. However, strains where only PBP2* is present were viable in both
207 *mecA⁺* and *mecA⁺ rpoB** (Fig. 3A to D). Both the PBP2 and PBP2* constructs were verified
208 by Western blot and Bocillin labelling (fig. S8D and E). Both strains with PBP2* were able to
209 grow with near parental (*mecA⁺* and *mecA⁺ rpoB**, respectively) cell morphology (fig. S9E
210 and F). All PBP2 and PBP2* constructs demonstrate a diminished cell size compared to
211 SH1000 (fig. S9H). Expression of PBP2* (lacking PBP2 transpeptidase activity) in the *mecA⁺*
212 or *mecA⁺ rpoB** backgrounds resulted in septa that exhibited the typical PG concentric-ring
213 architecture, with strands preferentially oriented in the circumferential direction (Fig. 3E and
214 F and fig. S10). We conclude that neither PBP2 nor PBP2a are responsible, even in part, for
215 the PG septal concentric rings associated with conventional cell division. Therefore, there are
216 two factors required for high-level MRSA: (i) PBP2a replaces the essential transpeptidase
217 activity of PBP2, and (ii) a *pot* mutation (e.g. *rpoB**) permits cell division without PBP1
218 transpeptidase activity.

219 **Potentiator mutations converge on nucleotide signalling**

220 Mutations in *rpoB* and *rpoC* have been associated with clinically important high-level MRSA
221 strains and the conversion from hetero- to homogeneous resistance (13, 14, 23, 24). Other *pot*
222 mutations, such as *rel*, *clpXP*, *gdpP*, *pde2* and *lytH* have been uncovered in laboratory studies
223 and in some cases clinically (13). Whilst other mutations enhanced the MIC of *mecA⁺*, tested
224 in our defined SH1000 background with a single copy of *mecA* in the chromosome, only *rpoB*
225 and *rel* led to high-level resistance (table S1; MIC ≥ 256 $\mu\text{g ml}^{-1}$).

226 The *rel* gene encodes a key component of the stringent response (25) and whilst the gene is
227 conditionally essential, the *pot* mutant strain (*rel**) has a C-terminal truncation in the regulatory
228 domain of the Rel protein, and likely increases (p)ppGpp levels (26). The stringent response
229 has been previously implicated as having a major role in potentiating high-level MRSA (27)
230 and here we found the presence of *mecA⁺ rpoB** led to a significant increase in the levels of
231 the stringent response signalling molecules ppGpp and pppGpp (Fig. 4A). To determine the

232 relationship between the stringent response and the dual pathways to high-level MRSA we
233 investigated its ability to compensate for the loss of PBP1 transpeptidase activity (Fig. 4B).
234 The *rel** mutation was as effective as *rpoB** in compensating for the absence of PBP1
235 transpeptidase activity as judged by measurement of plating efficiency (Fig. 4B), implicating
236 the stringent response in the ability to grow and divide without septal PG concentric rings.

237 **Therapeutic development for MRSA**

238 To counter the emergence of MRSA, compounds have been identified that resensitize these
239 strains to β -lactams (28). These include clomiphene (29) and norgestimate (30), as well as
240 natural products including epicatechin gallate (ECg) (31) and spermine (32). Their mode of
241 action is mostly unknown and so we tested their effect, at concentrations that resensitize *mecA*⁺
242 *rpoB** and the other clinical MRSA strains to oxacillin but do not inhibit growth without
243 antibiotic (see Materials and Methods) (Fig. 4C to E). Clomiphene and spermine did not inhibit
244 the plating efficiency of *pbp1* rpoB** but did for both *mecA*⁺ *pbp2** and *mecA*⁺ *pbp2* rpoB**,
245 suggesting a link to the activity of PBP2a. Norgestimate impaired the plating efficiency of
246 *pbp1* rpoB** and *mecA*⁺ *pbp2** but not *mecA*⁺ *pbp2* rpoB**, demonstrating a potential cross-
247 talk between the co-dependent pathways (i.e., acquisition of *mecA* and a *pot* mutation) that lead
248 to resistance. ECg inhibited the plating efficiency of all three strains indicating that it may
249 affect an Aux factor required under all conditions. These observations further differentiate the
250 two resistance pathways and provide specific interventions able to dissect the new mode of cell
251 division uncovered here.

252 **Discussion**

253 We have revealed that the high-level resistance to β -lactam antibiotics exhibited by some
254 MRSA strains is linked to an alternative mode of cell division set within the context of wider
255 physiological adaptations (i.e., increased ppGpp and pppGpp) (Fig. 4F). The development of
256 high-level MRSA is a two-step process in which PBP2a compensates for the lack of native
257 PBP2 transpeptidase activity in the presence of β -lactam antibiotics (22). PBP2 is an essential
258 enzyme that is required for the synthesis of the dense mesh PG on the inside of the cell wall at
259 both the septum and the cell periphery. It is therefore the major PBP in terms of bulk PG
260 synthesis. PBP2a cannot compensate for the lack of PBP2 protein (specifically its
261 transglycosylase activity (22)). However, as PBPs can form dimers (33), PBP2/2a heterodimers
262 could allow both the multiple protein interactions of PBP2 (34) and PBP2a transpeptidase
263 activity required for PG synthesis. PBP1 has essential transpeptidase activity and operates with
264 its cognate transglycosylase FtsW (35). Here we show that PBP1 activity is responsible for the
265 formation of the concentric rings that are characteristic of septal PG. PBP2a cannot compensate
266 for the lack of PBP1 activity but *pot* mutations can. The *pot* mutations permit successful cell
267 division without septal PG rings in the presence of high levels of antibiotics (Fig. 4F). This
268 compensatory mechanism does not involve a replacement of PBP1 activity but rather
269 physiological adaptations that allow division without it. A question arises as to whether the
270 ability to divide without septal PG concentric rings in high-level MRSA strains evolved
271 specifically, in the context of antibiotic use, or whether it is part of a wider physiological
272 capability that is deployed under stressful conditions? Mutations in *rpo* genes are often found
273 associated with antibiotic and stress resistance in *S. aureus* and many other organisms (24, 36,
274 37). A survey of 1,429 MRSA (ST22) clinical strains revealed that ~10% had at least one point
275 mutation in genes coding for core RNAP subunits or σ factors (24). The current study now
276 links these mutations to the widely conserved stringent response, which is a key component in
277 bacterial responses to stress and growth perturbations (25). Our *rpoB** strains exhibit lower

278 growth rates compared to parental strains (14), which could, at least in-part, facilitate the
279 alternative mode of division.

280 Given the array of MRSA SCC mec types and clonal lineages, it is likely that the effects of *pot*
281 factors, such as *rpo**, are influenced by the genetic background (13). This provides both
282 complexity in unravelling the interplay between *pot* and *aux* factors but also an opportunity to
283 establish those common, underlying principles that underpin resistance. The resensitizing
284 agents also provide avenues to probe underlying molecular mechanisms. Our study has
285 revealed insights into antibiotic resistance and facets of cell division in *S. aureus*. It is by
286 studying these processes in tandem that we can understand basic mechanisms of the bacterial
287 cell cycle and reveal ways to control antibiotic resistance.

288 **References**

- 289 1. B. Ribeiro da Cunha, L. P. Fonseca, C. R. C. Calado, Antibiotic discovery: Where have we
290 come from, where do we go? *Antibiot.* **8**, 1-21 (2019).
- 291 2. Antimicrobial Resistance Collaborators, Global burden of bacterial antimicrobial resistance in
292 2019: a systematic analysis. *Lancet* **399**, 629–655 (2022).
- 293 3. S. Lakhundi, K. Zhang, Methicillin-resistant *Staphylococcus aureus*: Molecular
294 characterization, evolution, and epidemiology. *Clin. Microbiol. Rev.* **31**:10.1128/cmr.00020-18
295 (2018).
- 296 4. B. J. Hartman, A. Tomasz, Low-affinity penicillin-binding protein associated with beta-lactam
297 resistance in *Staphylococcus aureus*. *J. Bacteriol.* **158**, 513–516 (1984).
- 298 5. W. Vollmer, D. Blanot, M. A. De Pedro, Peptidoglycan structure and architecture. *FEMS*
299 *Microbiology Reviews* **32**, 149–167 (2008).
- 300 6. L. Pasquina-Lemonche, J. Burns, R. D. Turner, S. Kumar, R. Tank, N. Mullin, J. S. Wilson, B.
301 Chakrabarti, P. A. Bullough, S. J. Foster, J. K. Hobbs, The architecture of the Gram-positive
302 bacterial cell wall. *Nature* **582**, 294–297 (2020).
- 303 7. S. F. Pereira, A. O. Henriques, M. G. Pinho, H. de Lencastre, A. Tomasz, Role of PBP1 in cell
304 division of *Staphylococcus aureus*. *J. Bacteriol.* **189**, 3525–3531 (2007).
- 305 8. K. Wacnik, V. A. Rao, X. Chen, L. Lafage, M. Pazos, S. Booth, W. Vollmer, J. K. Hobbs, R.
306 J. Lewis, S. J. Foster, Penicillin-Binding Protein 1 (PBP1) of *Staphylococcus aureus* has
307 multiple essential functions in cell division. *mBio.* **13**, e00669 (2022).
- 308 9. M. G. Pinho, S. R. Filipe, H. de Lencastre, A. Tomasz, Complementation of the essential
309 peptidoglycan transpeptidase function of penicillin-binding protein 2 (PBP2) by the drug
310 resistance protein PBP2A in *Staphylococcus aureus*. *J. Bacteriol.* **183**, 6525–6531 (2001).
- 311 10. E. García-Fernández, G. Koch, R. M. Wagner, A. Fekete, S. T. Stengel, J. Schneider, B.
312 Mielich-Süss, S. Geibel, S. M. Markert, C. Stigloher, D. Lopez, Membrane microdomain
313 disassembly inhibits MRSA antibiotic resistance. *Cell* **171**, 1354-1367.e20 (2017).
- 314 11. L. H. Otero, A. Rojas-Altuve, L. I. Llarrull, C. Carrasco-López, M. Kumarasiri, E. Lastochkin,
315 J. Fishovitz, M. Dawley, D. Heseck, M. Lee, J. W. Johnson, J. F. Fisher, M. Chang, S.
316 Mobashery, J. A. Hermoso, How allosteric control of *Staphylococcus aureus* penicillin binding
317 protein 2a enables methicillin resistance and physiological function. *PNAS* **110**, 16808-16813
318 (2013).
- 319 12. B. J. Hartman and, A. Tomasz, Expression of methicillin resistance in heterogeneous strains of
320 *Staphylococcus aureus*. *Antimicrob. Agents Chemother.* **29**, 85–92 (1986).
- 321 13. B. L. Bilyk, V. V. Panchal, M. Tinajero-Trejo, J. K. Hobbs, S. J. Foster, An Interplay of
322 multiple positive and negative factors governs methicillin resistance in *Staphylococcus aureus*.
323 *Microbiol. Mol. Biol. Rev.* **86**, e00159 (2022).
- 324 14. V. V. Panchal, C. Griffiths, H. Mosaei, B. Bilyk, J. A. F. Sutton, O. T. Carnell, D. P. Hornby,
325 J. Green, J. K. Hobbs, W. L. Kelley, N. Zenkin, S. J. Foster, Evolving MRSA: High-level β -
326 lactam resistance in *Staphylococcus aureus* is associated with RNA Polymerase alterations and
327 fine tuning of gene expression. *PLOS Pathog.* **16**, e1008672 (2020).
- 328 15. B. Salamaga, L. Kong, L. Pasquina-Lemonche, L. Lafage, M. von Und Zur Muhlen, J. F.
329 Gibson, D. Grybchuk, A. K. Tooke, V. Panchal, E. J. Culp, E. Tatham, M. E. O’Kane, T. E.
330 Catley, S. A. Renshaw, G. D. Wright, P. Plevka, P. A. Bullough, A. Han, J. K. Hobbs, S. J.
331 Foster, Demonstration of the role of cell wall homeostasis in *Staphylococcus aureus* growth
332 and the action of bactericidal antibiotics. *PNAS* **118**, 1-8 (2021).

- 333 16. R. D. Turner, E. C. Ratcliffe, R. Wheeler, R. Golestanian, J. K. Hobbs, S. J. Foster,
334 Peptidoglycan architecture can specify division planes in *Staphylococcus aureus*. *Nat.*
335 *Commun.* **1**, 26 (2010).
- 336 17. S. R. Harris, E. J. Feil, M. T. G. Holden, M. A. Quail, E. K. Nickerson, N. Chantratita, S.
337 Gardete, A. Tavares, N. Day, J. A. Lindsay, J. D. Edgeworth, H. De Lencastre, J. Parkhill, S.
338 J. Peacock, S. D. Bentley, Evolution of MRSA during hospital transmission and
339 intercontinental spread. *Science* **327**, 469–474 (2010).
- 340 18. M. T. G. Holden, E. J. Feil, J. A. Lindsay, S. J. Peacock, N. P. J. Day, M. C. Enright, T. J.
341 Foster, C. E. Moore, L. Hurst, R. Atkin, A. Barron, N. Bason, S. D. Bentley, C. Chillingworth,
342 T. Chillingworth, C. Churcher, L. Clark, C. Corton, A. Cronin, J. Doggett, L. Dowd, T.
343 Feltwell, Z. Hance, B. Harris, H. Hauser, S. Holroyd, K. Jagels, K. D. James, N. Lennard, A.
344 Line, R. Mayes, S. Moule, K. Mungall, D. Ormond, M. A. Quail, E. Rabinowitsch, K.
345 Rutherford, M. Sanders, S. Sharp, M. Simmonds, K. Stevens, S. Whitehead, B. G. Barrell, B.
346 G. Spratt, J. Parkhill, Complete genomes of two clinical *Staphylococcus aureus* strains:
347 Evidence for the evolution of virulence and drug resistance. *PNAS* **101**, 9786–9791 (2004).
- 348 19. T. Takano, W. C. Hung, M. Shibuya, W. Higuchi, Y. Iwao, A. Nishiyama, I. Reva, O. E.
349 Khokhlova, S. Yabe, K. Ozaki, M. Takano, T. Yamamoto, A new local variant (ST764) of the
350 globally disseminated ST5 lineage of hospital-associated methicillin-resistant *Staphylococcus*
351 *aureus* (MRSA) carrying the virulence determinants of community-associated MRSA.
352 *Antimicrob. Agents Chemother.* **57**, 1589–1595 (2013).
- 353 20. B. A. Diep, S. R. Gill, R. F. Chang, T. H. Van Phan, J. H. Chen, M. G. Davidson, F. Lin, J. Lin,
354 H. A. Carleton, E. F. Mongodin, G. F. Sensabaugh, F. Perdreau-Remington, Complete genome
355 sequence of USA300, an epidemic clone of community-acquired methicillin-resistant
356 *Staphylococcus aureus*. *Lancet* **367**, 731–739 (2006).
- 357 21. M. G. Pinho, S. R. Filipe, H. De Lencastre, A. Tomasz, Complementation of the essential
358 peptidoglycan transpeptidase function of penicillin-binding protein 2 (PBP2) by the drug
359 resistance protein PBP2A in *Staphylococcus aureus*. *J. Bacteriol.* **183**, 6525–6531 (2001).
- 360 22. M. G. Pinho, H. de Lencastre, A. Tomasz, An acquired and a native penicillin-binding protein
361 cooperate in building the cell wall of drug-resistant staphylococci. *PNAS* **98**, 10886-10891
362 (2001).
- 363 23. Y. Aiba, Y. Katayama, T. Hishinuma, H. Murakami-Kuroda, L. Cui, K. Hiramatsu, Mutation
364 of RNA polymerase β -subunit gene promotes heterogeneous-to-homogeneous conversion of β -
365 lactam resistance in methicillin-resistant *Staphylococcus aureus*. *Antimicrob. Agents*
366 *Chemother.* **57**, 4861–4871 (2013).
- 367 24. A. Krishna, B. Liu, S. J. Peacock, S. Wigneshweraraj, The prevalence and implications of single
368 nucleotide polymorphisms in genes encoding the RNA polymerase of clinical isolates of
369 *Staphylococcus aureus*. *MicrobiologyOpen* **9**, e1058 (2020).
- 370 25. S. E. Irving, N. R. Choudhury, R. M. Corrigan, The stringent response and physiological roles
371 of (pp)pGpp in bacteria. *Nat. Rev. Microbiol.* **19**, 256–271 (2021).
- 372 26. A. T. Deventer, D. Bryson, M. Shortill, A. B. Boraston, J. K. Hobbs, Molecular characterization
373 of clinical rel mutations and consequences for resistance expression and fitness in
374 *Staphylococcus aureus*. *Antimicrob. Agents Chemother.* **66**, e00938 (2022).
- 375 27. C. Kim, M. Mwangi, M. Chung, C. Milheirico, H. de Lencastre, A. Tomasz, The mechanism
376 of heterogeneous beta-lactam resistance in MRSA: key role of the stringent stress response.
377 *PLoS One* **8**, e82814 (2013).
- 378 28. T. J. Foster, Can beta-Lactam antibiotics be resurrected to combat MRSA? *Trends Microbiol.*
379 **27**, 26–38 (2019).

- 380 29. M. A. Farha, T. L. Czarny, C. L. Myers, L. J. Worrall, S. French, D. G. Conrady, Y. Wang, E.
381 Oldfield, N. C. Strynadka, E. D. Brown, Antagonism screen for inhibitors of bacterial cell wall
382 biogenesis uncovers an inhibitor of undecaprenyl diphosphate synthase. *PNAS* **112**, 11048–
383 11053 (2015).
- 384 30. Y. Yoshii, K. I. Okuda, S. Yamada, M. Nagakura, S. Sugimoto, T. Nagano, T. Okabe, H.
385 Kojima, T. Iwamoto, K. Kuwano, Y. Mizunoe, Norgestimate inhibits staphylococcal biofilm
386 formation and resensitizes methicillin-resistant *Staphylococcus aureus* to β -lactam antibiotics.
387 *npj Biofilms Microbiomes* **3**, 18 (2017).
- 388 31. P. D. Stapleton, S. Shah, K. Ehlert, Y. Hara, P. W. Taylor, The β -lactam-resistance modifier
389 (–)-epicatechin gallate alters the architecture of the cell wall of *Staphylococcus aureus*.
390 *Microbiology* **153**, 2093–2103 (2007).
- 391 32. D. H. Kwon, C. D. Lu, Polyamine effects on antibiotic susceptibility in bacteria. *Antimicrob.*
392 *Agents Chemother.* **51**, 2070–2077 (2007).
- 393 33. J. F. Fisher, S. Mobashery, β -Lactams against the Fortress of the Gram-Positive *Staphylococcus*
394 *aureus* Bacterium. *Chem. Rev.* **121**, 3412–3463 (2021).
- 395 34. V. R. Steele, A. L. Bottomley, J. Garcia-Lara, J. Kasturiarachchi, S. J. Foster, Multiple essential
396 roles for EzrA in cell division of *Staphylococcus aureus*. *Mol. Microbiol.* **80**, 542–555 (2011).
- 397 35. N. T. Reichmann, A. C. Tavares, B. M. Saraiva, A. Jouselin, P. Reed, A. R. Pereira, J. M.
398 Monteiro, R. G. Sobral, M. S. VanNieuwenhze, F. Fernandes, M. G. Pinho, SEDS-bPBP pairs
399 direct lateral and septal peptidoglycan synthesis in *Staphylococcus aureus*. *Nat. Microbiol.* **4**,
400 1368–1377 (2019).
- 401 36. L. Ostrer, Y. Ji, A. Khodursky, Identification and characterization of pleiotropic high-
402 persistence mutations in the beta subunit of the bacterial RNA polymerase. *Antimicrob. Agents*
403 *Chemother.* **65**, 00522 (2021).
- 404 37. J. A. Leeds, M. Sachdeva, S. Mullin, S. W. Barnes, A. Ruzin, In vitro selection, via serial
405 passage, of *Clostridium difficile* mutants with reduced susceptibility to fidaxomicin or
406 vancomycin. *J. Antimicrob. Chemother.* **69**, 41–44 (2014).
- 407 38. <https://doi.org/10.15131/shef.data.26341735>
- 408 39. R. M. Corrigan, L. Bowman, A. R. Willis, V. Kaeffer, A. Grundling, Cross-talk between two
409 nucleotide-signaling pathways in *Staphylococcus aureus*. *J. Biol. Chem.* **290**, 5826–5839
410 (2015).
- 411 40. R. P. Novick, S. I. Morse, In vivo transmission of drug resistance factors between strains of
412 *Staphylococcus aureus*. *J. Exp. Med.* **125**, 45–59 (1967).
- 413 41. S. Schenk, R. A. Laddaga, Improved method for electroporation of *Staphylococcus aureus*.
414 *FEMS Microbiol. Lett.* **94**, 133–138 (1992).
- 415 42. J. Schindelin, I. Arganda-Carreras, E. Frise, V. Kaynig, M. Longair, T. Pietzsch, S. Preibisch,
416 C. Rueden, S. Saalfeld, B. Schmid, J. Y. Tinevez, D. J. White, V. Hartenstein, K. Eliceiri, P.
417 Tomancak, A. Cardona, Fiji: an open-source platform for biological-image analysis. *Nat.*
418 *Methods* **9**, 676–682 (2012).
- 419 43. J. G. Beton, R. Moorehead, L. Helfmann, R. Gray, B. W. Hoogenboom, A. P. Joseph, M. Topf,
420 A. L. B. Pyne, TopoStats - A program for automated tracing of biomolecules from AFM
421 images. *Methods* **193**, 68–79 (2021).
- 422 44. T. Lindeberg, Edge Detection and Ridge Detection with Automatic Scale Selection. *Int. J.*
423 *Comput. Vis.* **30**, 117–156 (1998).
- 424 45. F. Meyer, Topographic distance and watershed lines. *Signal Processing* **38**, 113–125 (1994).

- 425 46. <https://doi.org/10.5281/zenodo.13082796>
- 426 47. <https://doi.org/10.5281/zenodo.13133978>
- 427 48. S. Berg, D. Kutra, T. Kroeger, C. N. Strachle, B. X. Kausler, C. Haubold, M. Schiegg, J. Ales,
428 T. Beier, M. Rudy, K. Eren, J. I. Cervantes, B. Xu, F. Beuttenmueller, A. Wolny, C. Zhang, U.
429 Koethe, F. A. Hamprecht, A. Kreshuk, ilastik: interactive machine learning for (bio)image
430 analysis. *Nat. Methods* **16**, 1226–1232 (2019).
- 431 49. <https://doi.org/10.5281/zenodo.13134076>
- 432 50. M. J. Horsburgh, J. L. Aish, I. J. White, L. Shaw, J. K. Lithgow, S. J. Foster, δ b modulates
433 virulence determinant expression and stress resistance: Characterization of a functional rsbU
434 strain derived from *Staphylococcus aureus* 8325-4. *J. Bacteriol.* **184**, 5457–5467 (2002).
- 435 51. W. M. Shafer, J. J. Landolo, Genetics of staphylococcal enterotoxin B in methicillin-resistant
436 isolates of *Staphylococcus aureus*. *Infect. Immun.* **25**, 902–911 (1979).
- 437 52. B. N. Kreiswirth, S. Löfdahl, M. J. Betley, M. O'reilly, P. M. Schlievert, M. S. Bergdoll, R. P.
438 Novick, The toxic shock syndrome exotoxin structural gene is not detectably transmitted by a
439 prophage. *Nature* **305**, 709–712 (1983).
- 440 53. C. Y. Lee, S. L. Buranen, Y. Zhi-Hai, Construction of single-copy integration vectors for
441 *Staphylococcus aureus*. *Gene* **103**, 101–105 (1991).
- 442 54. G. McVicker, T. K. Prajsnar, A. Williams, N. L. Wagner, M. Boots, S. A. Renshaw, S. J. Foster,
443 Clonal expansion during *Staphylococcus aureus* infection dynamics reveals the effect of
444 antibiotic intervention. *PLoS Pathog.* **10**, e1003959 (2014).
- 445 55. P. D. Fey, J. L. Endres, V. K. Yajjala, T. J. Widhelm, R. J. Boissy, J. L. Bose, K. W. Bayles, A
446 genetic resource for rapid and comprehensive phenotype screening of nonessential
447 *Staphylococcus aureus* genes. *mBio.* **4**, 00537 (2013).
- 448 56. R. M. Corrigan, J. C. Abbott, H. Burhenne, V. Kaefer, A. Grundling, c-di-AMP is a new second
449 messenger in *Staphylococcus aureus* with a role in controlling cell size and envelope stress.
450 *PLoS Pathog.* **7**, e1002217 (2011).
- 451 57. V. A. Lund, K. Wacnik, R. D. Turner, B. E. Cotterell, C. G. Walther, S. J. Fenn, F. Grein, A. J.
452 M. Wollman, M. C. Leake, N. Olivier, A. Cadby, S. Mesnage, S. Jones, S. J. Foster, Molecular
453 coordination of *Staphylococcus aureus* cell division. *eLife* **7**, e32057 (2018).
- 454 58. M. Arnaud, A. Chastanet, M. Débarbouillé, New vector for efficient allelic replacement in
455 naturally nontransformable, low-GC-content, gram-positive bacteria. *Appl. Environ.*
456 *Microbiol.* **70**, 6887–6891 (2004).

457 Acknowledgements

458 We are grateful to Nicholas Mullin, Xinyue Chen, Anaam Alomari, Viralkumar V. Panchal,
459 Bartek Salamaga, and Matthew J. Barker for helpful discussions, also Jodi Lindsay (St.
460 George's UCL) and James O'Gara (University of Galway) for provision of strains. Electron
461 Microscopy was carried out at the School of Biosciences Cryo-Electron Microscopy Facility,
462 University of Sheffield. Fluorescence microscopy was performed at the Wolfson Light
463 Microscopy Facility, University of Sheffield. The research was in part carried out at the
464 National Institute for Health and Care Research (NIHR) Sheffield Biomedical Research Centre
465 (BRC). For the purpose of open access, the authors have applied a CC BY public copyright
466 license to any author accepted manuscript version arising from this submission. **Funding:** This
467 work was supported by the Engineering and Physical Sciences Research Council (grant
468 EP/T002778/1 to J.K.H. and S.J.F), the Wellcome Trust (grants 212197/Z/19/Z to J.K.H and
469 S.J.F and 104110/Z/14/A to J.K.H., S.J.F., J.G. and R.M.C) and the Biotechnology and

470 Biological Sciences Research Council (grant BB/R018383/1 to WMD). **Author**
471 **contributions:** A.F.A.-O, and K.W designed the study, performed experiments, analysed, and
472 interpreted data, and wrote the manuscript. (A.F.A.-O.: Figs. 1, 2, 3, Supplementary Materials
473 Figs. S1-S3, S6 & S10; K.W.: Figs. 2-4, Supplementary Materials Figs. S4-S9). L.L., M.T.-T.,
474 B.B., S.E.I., J.A.F.S and C.J.P.-R. performed the experiments, analysed, and interpreted the
475 data (L.L. Fig. 1, Supplementary Materials: Figs. S4 & S6; M.T.-T.: Fig. 4, Supplementary
476 Materials Figs. S4, S8, S10; S.E.I.: Fig. 4; J.A.F.S.: Supplementary Materials: Fig. S3 & Table
477 S1 and C.J.P.-R.: Supplementary Materials Fig. S10). L.P.-L. and D.S.O. developed the semi-
478 automated macro used to calculate cell volume measurements and L.P.-L analysed the data
479 (Supplementary Materials Figs. S4, S5 & S9). Also, L.P.-L. developed the semi-automated
480 macro used to calculate the cell wall pore area (Supplementary Materials Figs. S2, S6, S10).
481 S.A.R and E.B. performed the experiments and analyzed data (Supplementary Materials Fig.
482 S2). O.M. and W.M.D. developed Matlab-based software used for the fibre detection (Figs. 1-
483 3). D.J.H., J.F., R.C. and J.G. analysed and interpreted data, and wrote and reviewed the
484 manuscript. J.K.H. and S.J.F. designed the study, interpreted the data, wrote the manuscript
485 and directed the project. **Competing interests:** The authors declare no competing interests.
486 **Data and materials availability:** The data that support the findings of this study are available
487 in the Online Research Data (ORDA) figshare from the University of Sheffield with the
488 identifier (38).

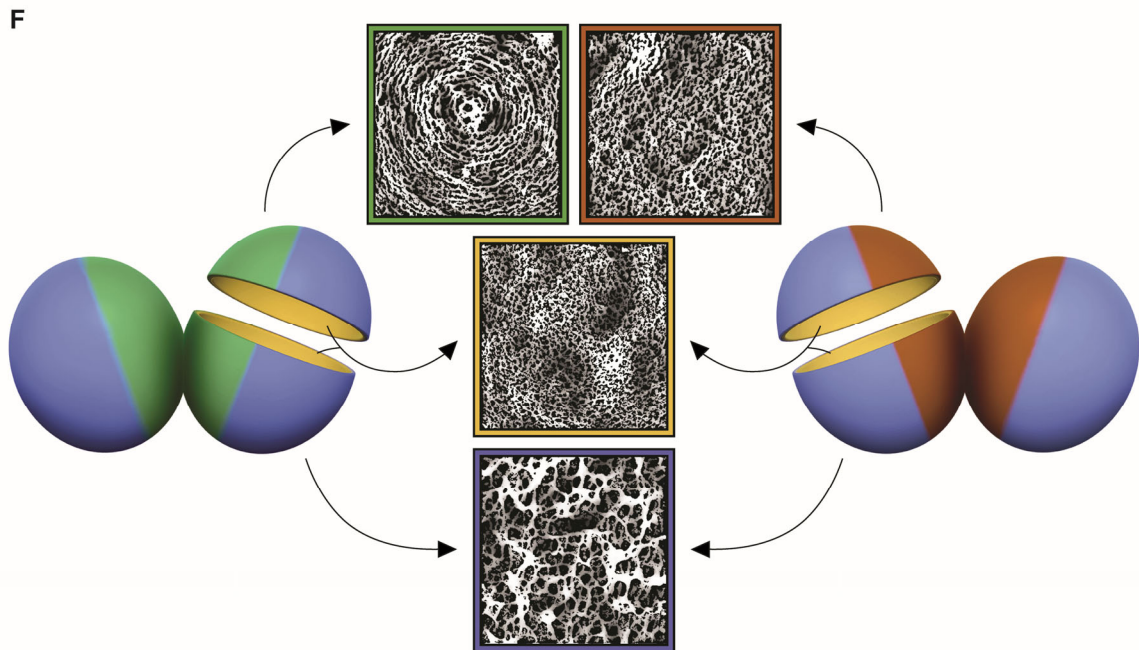
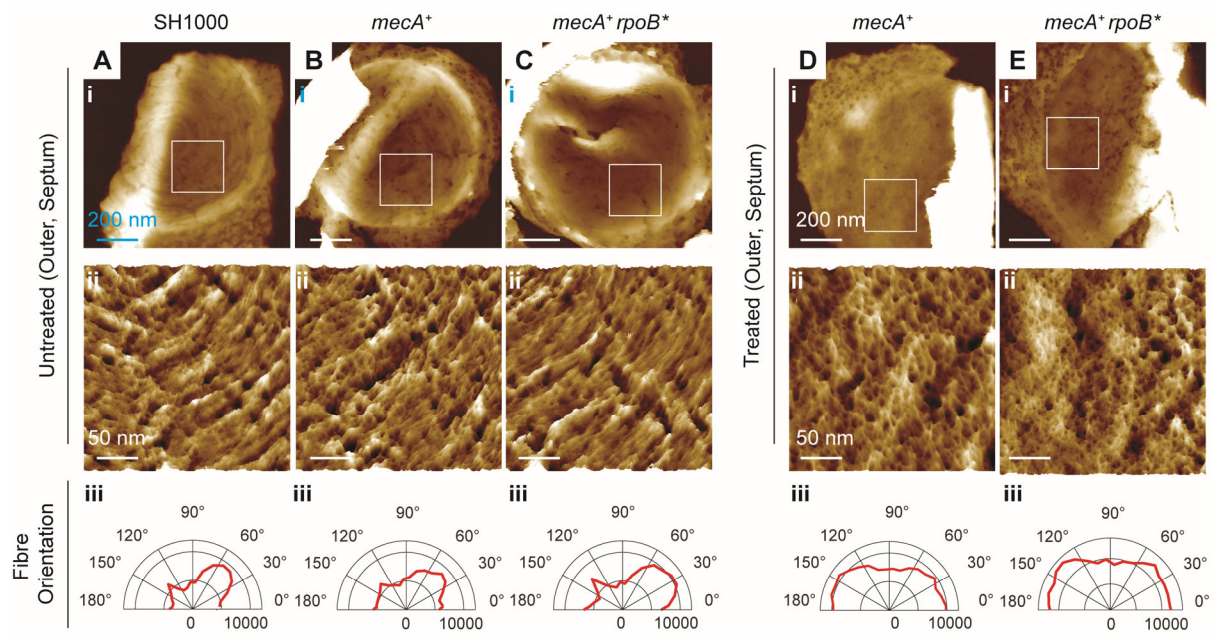
489 **Supplementary Materials**

490 Materials and Methods

491 Figs. S1 to S10

492 Tables S1 and S4

493 References (39 - 58)



494

495

496 **Fig. 1. Methicillin treatment of MRSA alters the architecture of the cell wall.** From left to

497 right, (A-C) show the outer surfaces of newly revealed septa, in samples of isolated sacculi of

498 untreated (A) SH1000, (B) *mecA*⁺, and (C) *mecA*⁺ *rpoB*^{*} respectively. (D-E) Show the outer

499 surface of the newly revealed septa of (D) *mecA*⁺ and (E) *mecA*⁺ *rpoB*^{*} treated with methicillin

500 (1.5 and 25 $\mu\text{g ml}^{-1}$ respectively). In all columns: (i) shows an individual fragment of sacculus

501 corresponding to the outer surface of the septum. Topographical height (z) range presented in

502 each of these images (from left to right) is 140, 140, 150, 120, and 185 nm. (ii) Shows pseudo-

503 three dimensional (3D) high resolution AFM images of the sections indicated by the white

504 boxes in (i). Topographical height (z) range presented in each of these images (from left to

505 right) is 7.5, 10, 7.5, 12, and 20 nm. (iii) Represents the combined angular histogram of fibre

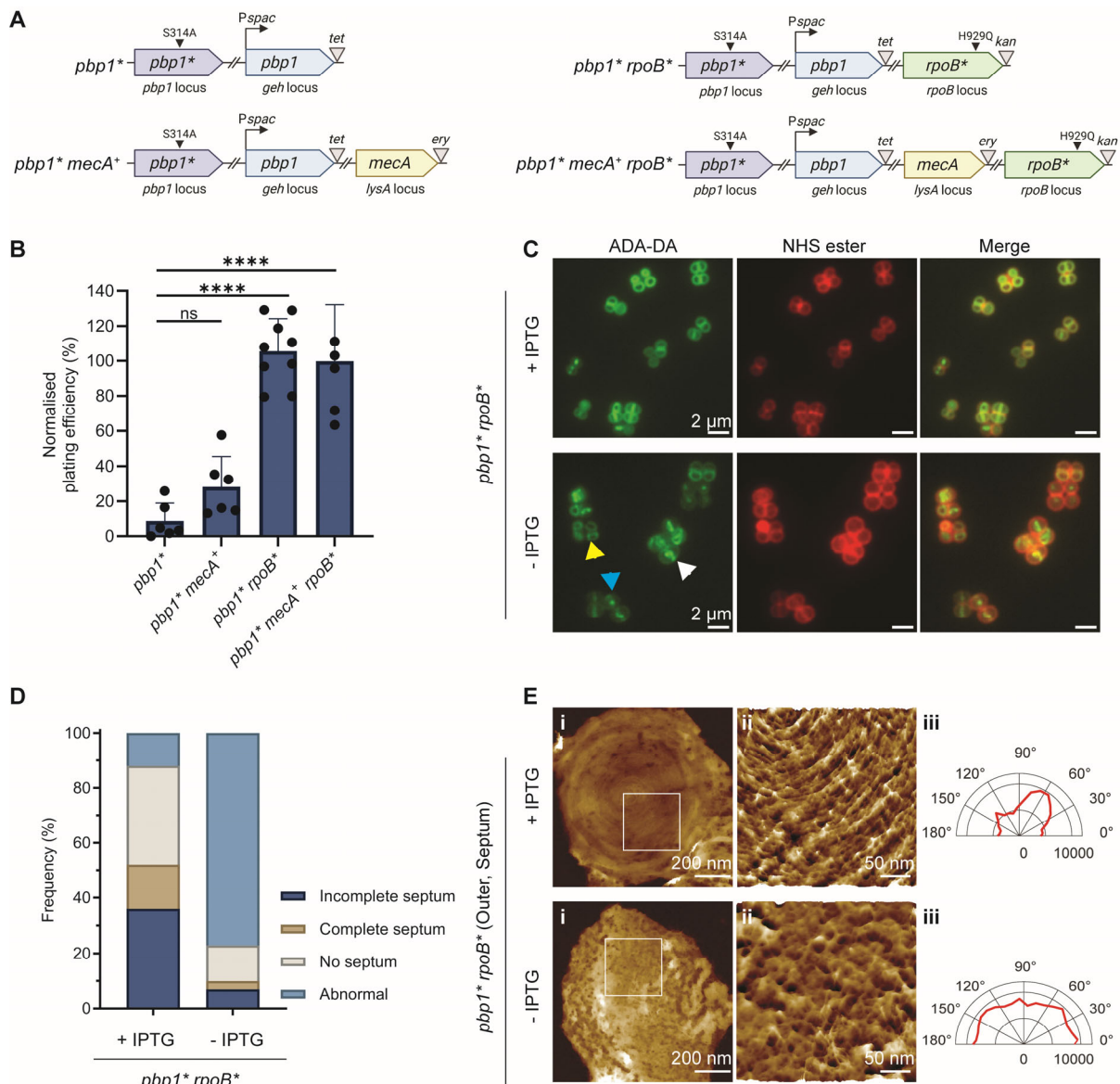
506 orientation of AFM high-resolution images similar to those in (ii). The fibre orientation

507 analysis method used for the orientation detection is described in the Materials and Methods

508 section. (F) Shows an interpretative diagram of different architectures (concentric rings, dense

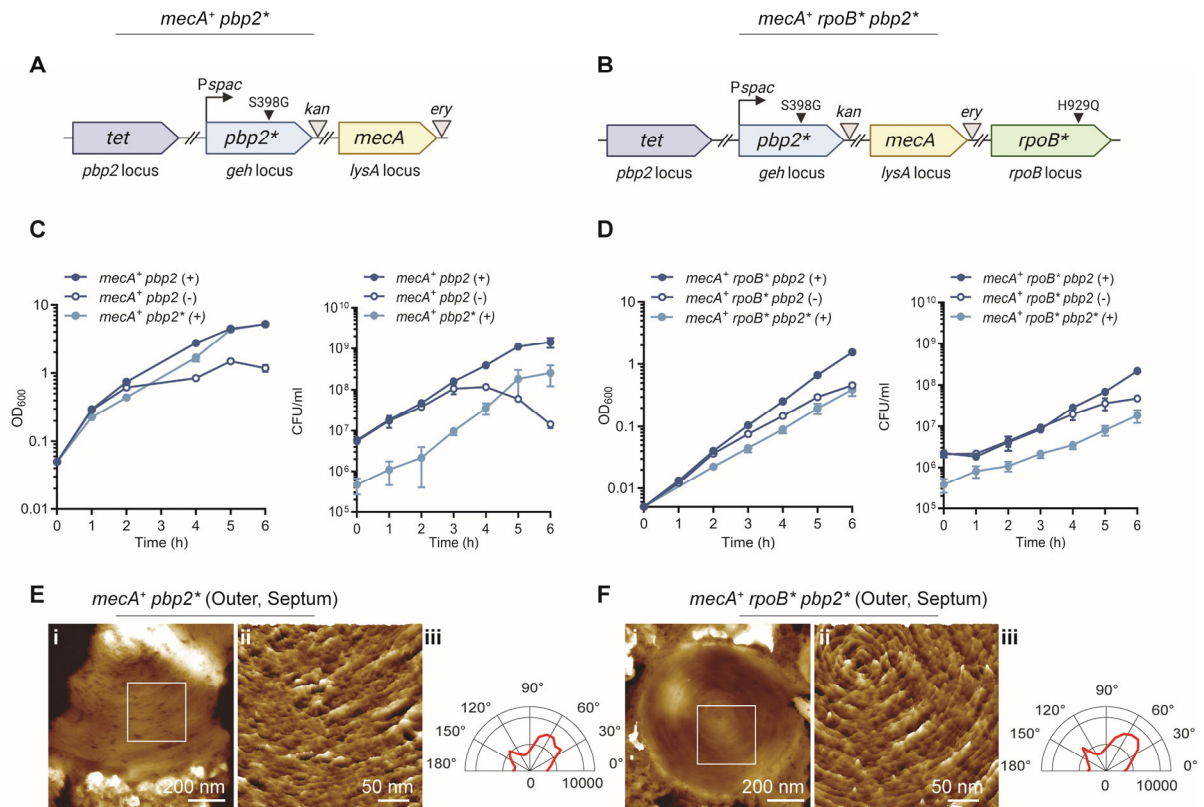
509 mesh, and open mesh) observed by high-resolution AFM on different surfaces (outer surface

509 of newly revealed septa, inner surface of the septa, and outer surface of cell periphery) of
510 untreated (left-hand side) and antibiotic treated (right-hand side) MRSA cell wall. The green
511 colour represents the concentric rings associated with the outer surface of the septum of
512 untreated cells, blue colour shows the open mesh at the cell periphery, yellow colour depicts
513 the dense mesh on the inner wall of the cell and lastly the brown colour represents the dense
514 mesh on the outer surface of the septum after treatment with methicillin. The modified AFM
515 images in Fig. 1F span 400 nm by 400 nm in x and y dimension.



516
 517 **Fig. 2. Loss of PBP1 transpeptidase activity can be compensated for by *rpoB*^{*} but not**
 518 ***mecA*⁺.** (A) Representation of *pbp1*^{*} genetic constructs. An ectopic *pbp1* copy, at the lipase
 519 (*geh*) locus is controlled by the *Pspac* promoter. The *pbp1* gene at its native locus has a point
 520 mutation (940T>G) resulting in inactivation of transpeptidase activity (S314A, *pbp1*^{*}). The
 521 *mecA*⁺ gene is expressed from its native promoter at the *lysA* locus. In *rpoB*^{*}, a point mutation
 522 results in an amino acid substitution (H929Q) in RpoB. *tet*, *ery* and *kan* represent tetracycline,
 523 erythromycin and kanamycin resistance cassettes, respectively. The graphics were created with
 524 BioRender.com. (B) Plating efficiency of *pbp1*^{*}, *pbp1*^{*} *mecA*⁺, *pbp1*^{*} *rpoB*^{*} and *pbp1*^{*} *mecA*⁺
 525 *rpoB*^{*} without IPTG. Plating efficiencies were compared to controls grown with IPTG, using
 526 a one-way ANOVA with Dunnett's multiple comparison test (ns, not significant; ****,
 527 *P* < 0.0001). Error bars show mean ± standard deviation (SD). (C) Fluorescence microscopy
 528 images of *pbp1*^{*} *rpoB*^{*} grown +/- IPTG for 4 h, labelled with ADA-DA (5 min) and then
 529 NHS-ester Alexa Fluor 555 to image nascent PG and cell wall, respectively. Images are z stack
 530 average intensity projections. Scale bars = 2 μm. (D) Quantification of cellular phenotypes
 531 based on ADA-DA incorporation in *pbp1*^{*} *rpoB*^{*} incubated with IPTG (+) or without IPTG
 532 (-), n = 511 and 654 (respectively). Examples of cells classified as abnormal with misshapen
 533 septal rings (yellow arrowhead), accumulation of ADA-DA at septal centre, 'plug' (blue
 534 arrowhead) and mislocalized ADA-DA incorporation (white arrowhead) are shown C. (E)

535 AFM images of newly exposed outer surface of the septum after cell division of *pbp1* rpoB**
536 grown +/- IPTG for 4 h, reveal lack of concentric-ring structures in -IPTG. (i) Representative
537 outer septal surfaces with height (z) range of 120 nm and the HS applies to both. (ii) Shows
538 pseudo-3D AFM high resolution images of the region within the white box in (i).
539 Topographical height (z) range (top) = 9.5 nm, and HS (bottom) = 21 nm. (iii) Represents the
540 combined angular histogram of fibre orientation of AFM high resolution images similar to
541 those in (ii).



542
543
544
545
546
547
548
549
550
551
552
553
554
555
556
557
558
559
560

Fig. 3. Loss of PBP2 transpeptidase activity can be compensated for by *mecA* but not *rpoB.** (A-B) Schematic representation of *mecA*⁺ *pbp2** (SJF5807) and *mecA*⁺ *rpoB** *pbp2** (SJF5809) genetic constructs. A copy of *pbp2* with an inactive transpeptidase domain (*pbp2**, 1191-1192TC>GG, S398G) was placed under the control of the *Pspac* promoter at the lipase (*geh*) locus of SH1000, *pbp2* at its native locus was then deleted (marked with *tet*). In both strains, a copy of a *mecA* gene expressed from its native promoter was located at the *lysA* locus. In *mecA*⁺ *rpoB** *pbp2** (SJF5809) the *rpoB* gene has a point mutation which results in H929Q (*rpoB**). *ery* and *kan* represent erythromycin and kanamycin resistance cassettes, respectively. The graphics in (A-B) were created with BioRender.com. (C) Growth curves of *mecA*⁺ *pbp2* (SJF5663) grown in the presence (+) or absence (-) of IPTG, and *mecA*⁺ *pbp2** (SJF5807) (+ IPTG). (D) Growth curves of *mecA*⁺ *rpoB** *pbp2* (SJF5674) grown in the presence (+) or absence (-) of IPTG, and *mecA*⁺ *rpoB** *pbp2** (SJF5809) (+ IPTG). (E-F) AFM images of the newly revealed outer surface of septa after cell division of *mecA*⁺ *pbp2** (SJF5807) and *mecA*⁺ *rpoB** *pbp2** (SJF5809), respectively. In both E and F, (i) shows the outer surface of a representative septum. Topographical height (*z*) range of 130 nm applies to both. (ii) Shows a pseudo-3D high resolution image of the region within the white box in (i). Height range are 12 nm for E(ii) and 7 nm for F(ii). (iii) Represents the combined angular histogram of fibre orientation of AFM high resolution images similar to images in (ii).

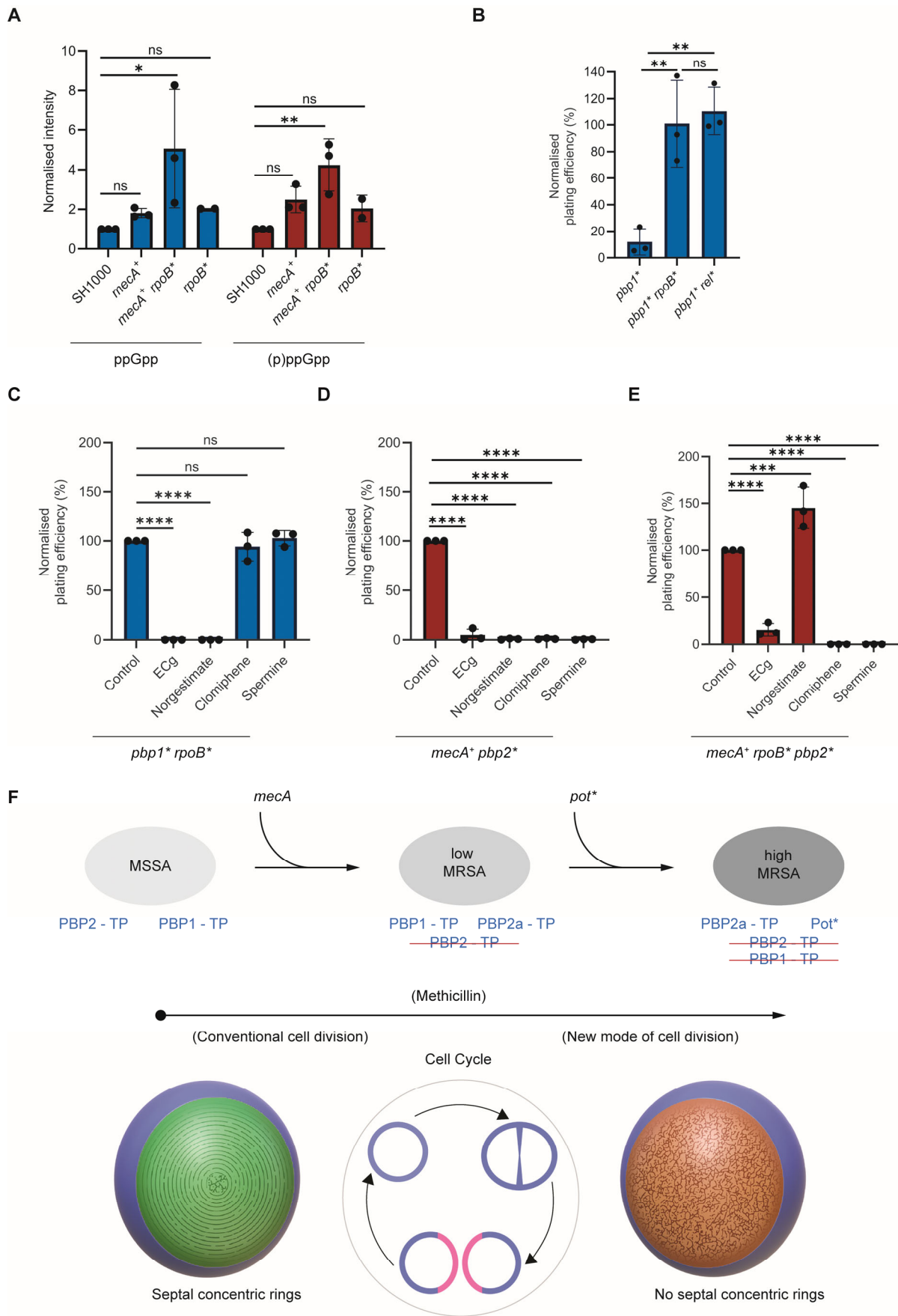


Fig. 4. Dual pathways to high-level MRSA. (A) Measurement of ppGpp and (p)ppGpp levels in SH1000, *mecA*⁺, *rpoB*^{*} and *mecA*⁺ *rpoB*^{*}, normalised to SH1000 and compared using one-

564 way ANOVA with Dunnett's multiple comparison test (ns, not significant; *, $P < 0.05$; **, $P < 0.01$). P values from left to right: 0.8727, 0.0425, 0.8290, 0.1470, 0.0051 and 0.4317. Error
565 bars show the mean \pm SD. (B) Plating efficiency of *pbp1**, *pbp1* rpoB** and *pbp1* rel* without
566 IPTG. Plating efficiency values were compared to controls with IPTG, using one-way ANOVA
567 with Tukey's multiple comparison test (**, left to right $P = 0.0049$ and 0.003). Error bars show
568 mean \pm SD. (C-E) Plating efficiency of (C) *pbp1* rpoB**, (D) *mecA⁺ pbp2** and (E) *mecA⁺*
569 *rpoB* pbp2** without IPTG supplemented with ECg, norgestimate, clomiphene or spermine.
570 Data were compared to no inhibitor plates (Control) using a one-way ANOVA with Dunnett's
571 multiple comparison test (ns, not significant; ****, $P < 0.0001$; ***, $P = 0.0004$). Error bars
572 show mean \pm SD from three independent biological repeats. (F) Model for high-level MRSA
573 development via acquisition of *mecA* and *pot* mutations (including *rpo** and *rel**), resulting in
574 low-level (low) and subsequently high-level (high) resistance. In MSSA, without methicillin,
575 PBP1 and PBP2 transpeptidases are active. In low-level MRSA, at intermediate methicillin
576 levels sufficient to kill MSSA, PBP2 transpeptidase is inhibited but complemented by PBP2a.
577 In high-level MRSA, at methicillin levels sufficient to kill MSSA and low-level MRSA, PBP2
578 and PBP1 transpeptidases are inhibited but complemented by PBP2a transpeptidase and Pot*,
579 respectively. PBP1 transpeptidase is responsible for the characteristic septal PG concentric
580 rings, during conventional cell division (green regions on blue cell background). In high-level
581 MRSA, in the presence of methicillin, septal PG concentric rings are replaced by mesh (brown
582 regions on blue cell background), revealing a novel mode of cell division requiring both PBP2a
583 and Pot*.
584

1



2

3

4

5

Supplementary Materials for

6

7

Two co-dependent routes lead to high-level MRSA

8

9 Abimbola Feyisara Adedeji-Olulana^{1†}, Katarzyna Wacnik^{2,3,†}, Lucia Lafage^{2,3}, Laia
10 Pasquina-Lemonche^{1,3}, Mariana Tinajero-Trejo^{2,3}, Joshua A. F. Sutton^{2,3}, Bohdan Bilyk^{2,3},
11 Sophie E. Irving^{2,3}, Callum J. Portman Ross^{2,3}, Oliver J. Meacock¹, Sam A. Randerson¹,
12 Ewan Beattie¹, David S. Owen², James Florence^{2,3}, William M. Durham¹, David J. Hornby^{2,3},
13 Rebecca M. Corrigan^{2,3}, Jeffrey Green^{2,3}, Jamie K. Hobbs^{1,*}, Simon J. Foster^{2,3,*}

14

15 Corresponding author. Email: jamie.hobbs@sheffield.ac.uk; s.foster@sheffield.ac.uk.

16 **The PDF file includes:**

17 Materials and Methods

18 Figs. S1 to S10

19 Tables S1 to S4

20 **Materials and Methods**

21 Bacterial growth conditions

22 The strains used in this study are listed in Table S2. *S. aureus* strains were grown in tryptic soy
23 broth (TSB), except for (p)ppGpp experiments which used low phosphate chemically defined
24 medium (39) (CDM), at 37°C with aeration. For solid, Tryptic Soy Agar media (TSA), 1.5%
25 (w/v) agar was added. When necessary, growth media were supplemented with kanamycin
26 (50 µg ml⁻¹), tetracycline (1 µg ml⁻¹), chloramphenicol (10 µg ml⁻¹), erythromycin (5 µg ml⁻¹),
27 lincomycin (25 µg ml⁻¹), methicillin (0.25, 1.5, 2, 25 or 40 µg ml⁻¹), isopropyl β-D-
28 thiogalactopyranoside (IPTG; 50 µM or 1 mM) or mupirocin (60 µg ml⁻¹). For *mecA*⁺ *pbp2*^{*}
29 (SJF5807) and *mecA*⁺ *rpoB*^{*} *pbp2*^{*} (SJF5809), 1 mM IPTG was added to growth media at all
30 times.

31 Construction of plasmids

32 *Escherichia coli* NEB5α was used for the construction of all plasmids. Correct plasmid
33 sequences were confirmed by DNA sequencing (Sanger sequencing by Source BioScience).
34 Plasmids and oligonucleotides used in this study are listed in Table S3 and Table S4,
35 respectively.

36 pKB-*Pspac-pbp2*

37 A fragment containing the full-length *pbp2* gene and its ribosome-binding site (RBS) was PCR
38 amplified (from SH1000) using pCQ11-*pbp2*-F/-R primers and cloned into AscI and NheI cut
39 pCQ11-FtsZ-SNAP by Gibson assembly, resulting in pCQ11-*pbp2*. Next, the fragment
40 containing the *Pspac* promoter, RBS and *pbp2* was PCR amplified from *S. aureus* SH1000
41 genomic DNA using pKB-*Pspac-pbp1*-F and pKB-*pbp2*-R and cloned into BamHI and EcoRI
42 cut pGM074, giving pKB-*Pspac-pbp2*.

43 pKB-*Pspac-pbp2*^{*}

44 A point mutation resulting in PBP2-TP inactivation (S398G) was introduced by site-directed
45 mutagenesis using *pbp2*TP-F/-R primers and Q5 Site Directed Mutagenesis kit (New England
46 Biolabs), creating pKB-*Pspac-pbp2*^{*}.

47 pMAD-Δ*pbp2*

48 One kb fragments upstream (up) and downstream (down) of *pbp2* were PCR amplified from *S.*
49 *aureus* SH1000 genomic DNA using pMAD-Δ*pbp2*-F and *pbp2*-up-R, and *pbp2*-down-F and
50 pMAD-Δ*pbp2*-R, respectively, while the tetracycline cassette (*tet*) was PCR amplified from
51 pAISH1 using *tetR-pbp2*-F/-R primers. The up, *tet* and down fragments were ligated into
52 EcoRI and BamHI cut pMAD by Gibson assembly, resulting in pMAD-Δ*pbp2*.

53 Construction of mutants

54 All plasmids were introduced into restrictive-deficient *S. aureus* RN4220 and moved to a final
55 *S. aureus* SH1000 strain by phage Φ11 transduction (40, 41). Whole genome sequencing was
56 provided by MicrobesNG.

57 *pbp1* rpoB** and Δ *pbp1 rpoB**

58 Strains containing *pbp1** (SJF4656, SH1000 *geh::Pspac-pbp1 pbp1::pbp1* lacI*) and Δ *pbp1*
59 (SJF5106, SH1000 *geh::Pspac-pbp1 Δ pbp1 lacI*) were transduced with a phage lysate from
60 SJF5046 (SH1000 *lysA::mecA rpoB^{H929Qkan}*), resulting in *pbp1* rpoB** and Δ *pbp1 rpoB**.

61 *pbp2*

62 The pKB-*Pspac-pbp2* plasmid was used to transform *S. aureus* CYL316. The chromosomal
63 fragment containing the plasmid integrated in the *geh* locus was moved by phage transduction
64 into SH1000, resulting in SH1000 *geh::Pspac-pbp2* (SJF4924). SJF4924 was then transformed
65 with pMAD- Δ *pbp2*. Chromosomal integration of the plasmid at 42°C and excision at 28°C led
66 to a marked deletion of *pbp2* (*pbp2::tet*). To provide a control of *Pspac-pbp2*, *lacI* was
67 introduced by transduction using a phage lysate of VF17 (SH1000 *lacI*), resulting in the *pbp2*
68 mutant (SJF5630, SH1000 *geh::Pspac-pbp2 pbp2::tet lacI*).

69 *mecA⁺ pbp2* and *mecA⁺ rpoB* pbp2*

70 *Pspac-pbp2* from SJF4924 was transduced into *mecA⁺* (SJF4996, SH1000 *lysA::mecA*) and
71 *mecA⁺ rpoB** (SJF5003, SH1000 *lysA::mecA rpoB^{H929Q}*). Next, *pbp2* was deleted by
72 transducing *pbp2::tet* from SJF5630. Finally, *lacI* from VF17 was added, creating *mecA⁺ pbp2*
73 (SJF5663, SH1000 *lysA::pmecA geh::Pspac-pbp2 pbp2::tet lacI*) and *mecA⁺ rpoB* pbp2*
74 (SJF5674, SH1000 *lysA::pmecA rpoB^{H929Q} geh::Pspac-pbp2 pbp2::tet lacI*).

75 *rpoB* pbp2*

76 In the *rpoB** mutant (SJF5010, SH1000 *lysA::kan rpoB^{H929Q}*), the kanamycin resistance
77 cassette in the *lysA* locus was swapped for the erythromycin resistance cassette by phage
78 transduction of *lysA::ery* from GMSA015 (SH1000 *lysA::ery*). Next, *Pspac-pbp2* from
79 SJF4924, *pbp2::tet* from SJF5630 and *lacI* from VF17 were added, resulting in *rpoB* pbp2*
80 (SJF5690, SH1000 *lysA::ery rpoB^{H929Q} geh::Pspac-pbp2 pbp2::tet*).

81 *mecA⁺ pbp2** and *mecA⁺ rpoB* pbp2*

82 *S. aureus* CYL316 was transformed with pKB-*Pspac-pbp2**. The chromosomal fragment
83 carrying the integrated plasmid (*geh::Pspac-pbp2**) was transduced into *mecA⁺* (SJF4996) and
84 *mecA⁺ rpoB** (SJF5003). Next, *pbp2* was deleted by transducing *pbp2::tet* from SJF5630.
85 Finally, *lacI* from VF17 was added, giving *mecA⁺ pbp2** (SJF5807, SH1000 *lysA::pmecA*
86 *geh::Pspac-pbp2* pbp2::tet lacI*) and (SJF5809, SH1000 *lysA::pmecA rpoB^{H929Q} geh::Pspac-*
87 *pbp2* pbp2::tet lacI*).

88 *gdpP*, *lytH*, *pde2*, *clpP*, *clpX* and *rel*

89 SH1000 was transduced with a phage lysate from ANG1959 (SEJ1 *gdpP::kan*), NE1369 (JE2
90 *lytH::Tn*), NE1208 (JE2 *pde2::Tn*) or NE1714 (JE2 *rel::Tn*), resulting in *gdpP* (SJF5025,
91 SH1000 *gdpP::kan*), *lytH* (SJF5455, SH1000 *lytH::Tn*), *pde2* (SJF5454, SH1000 *pde2::Tn*),
92 *clpP* (SH1000 *clpP::Tn*), *clpX* (SH1000 *clpX::Tn*) and *rel* (SJF5457, SH1000 *rel::Tn*),
93 respectively.

94 *mecA⁺ gdpP, mecA⁺ lytH, mecA⁺ pde2, mecA⁺ clpP, mecA⁺ clpX and mecA⁺ rel*

95 The *mecA⁺* mutant (SJF4996, SH1000 *lysA::mecA*) was transduced with a phage lysate from
96 ANG195 (SEJ1 *gdpP::kan*), giving *mecA⁺ gdpP* (SJF5464, SH1000 *lysA::mecA gdpP::kan*).

97 SJF5324 (SH1000 *geh::mecA lysA::tet*) was transduced with a phage lysate from NE1369 (JE2
98 *lytH::Tn*), NE1208 (JE2 *pde2::Tn*) or NE1714 (JE2 *rel::Tn*), resulting in *mecA⁺ lytH* (SJF5461,
99 SH1000 *geh::mecA lysA::tet lytH::Tn*), *mecA⁺ pde2* (SJF5460, SH1000 *geh::mecA lysA::tet*
100 *pde2::TN*), *mecA⁺ clpP* (SH1000 *geh::mecA, clpP::Tn*), *mecA⁺ clpX* (SH1000 *geh::mecA,*
101 *clpX::Tn*) and *mecA⁺ rel* (SJF5463, SH1000 *geh::mecA lysA::tet rel::Tn*), respectively.

102 Directed evolution of high-level resistant MRSA strains

103 Using our previous approach (14), EMRSA15 and USA300 (minimal inhibitory concentration,
104 MIC 16-24 and 0.75 $\mu\text{g ml}^{-1}$, respectively) were plated on gradients of oxacillin (0-256
105 $\mu\text{g ml}^{-1}$) to select for high-level resistant derivatives. High level resistant clones (EMRSA15
106 (HL) and USA300 (HL), MIC >256 $\mu\text{g ml}^{-1}$ oxacillin for both) were picked and subjected to
107 whole genome sequencing. This revealed 3 single nucleotide polymorphisms (SNPs) for
108 USA300 (HL) (resulting in protein alterations LysS G429S, LysS R430H and
109 SAUSA300_0212 Q141*) and a total of 13 SNPs in 10 different genes for EMRSA15 (HL).

110 *pbp1* rel*

111 The *pbp1** mutant (SJF4656, SH1000 *geh::Pspac-pbp1 pbp1::pbp1* lacI*) was transduced
112 with a lysate from NE1714 (JE2 *rel::Tn*), giving *pbp1* rel* (SJF5513, SH1000 *geh::Pspac-*
113 *pbp1 pbp1::pbp1* lacI rel::Tn*).

114 Plating efficiency

115 Cells were grown from an OD₆₀₀ of 0.1 in TSB supplemented with 10 $\mu\text{g ml}^{-1}$ chloramphenicol
116 and 50 μM IPTG to early exponential phase (OD₆₀₀ ~0.3-0.5). Cells were then washed three
117 times in phosphate-buffered saline (PBS) and a dilution series of cell suspensions were plated
118 onto TSA containing 10 $\mu\text{g ml}^{-1}$ chloramphenicol, with or without 1 mM IPTG. For
119 experiments with sensitizing compounds, *pbp1* rpoB** (SJF5306) was grown as described
120 above and plated on TSA containing 10 $\mu\text{g ml}^{-1}$ chloramphenicol and a sensitizing compound.
121 *mecA⁺ pbp2** (SJF5807) and *mecA⁺ rpoB* pbp2** (SJF5809) were grown in TSB supplemented
122 with 10 $\mu\text{g ml}^{-1}$ chloramphenicol and 1 mM IPTG to exponential phase (OD₆₀₀ ~0.5) and plated
123 on TSA containing 10 $\mu\text{g ml}^{-1}$ chloramphenicol, 1 mM IPTG and a sensitizing
124 compound. Relative plating efficiency was expressed as the number of cells on plates without
125 IPTG, compared to the number of cells from plates with IPTG, multiplied by 100.

126 Depletion of PBP1 or PBP2

127 *Pspac-pbp1* and *Pspac-pbp2* containing strains were grown from an OD₆₀₀ of 0.1 to the
128 exponential phase (OD₆₀₀ ~0.3-0.5) in TSB supplemented with 10 $\mu\text{g ml}^{-1}$ chloramphenicol
129 and 50 μM IPTG. Cells were then washed three times by centrifugation and resuspension in
130 TSB and inoculated in fresh TSB containing 10 $\mu\text{g ml}^{-1}$ chloramphenicol to an OD₆₀₀ of 0.05
131 for phenotypic analysis, or to an OD₆₀₀ of 0.005 for growth studies. Control samples (+IPTG)
132 were grown in TSB supplemented with 10 $\mu\text{g ml}^{-1}$ chloramphenicol and 1 mM IPTG at all
133 times.

134 Growth in methicillin

135 High-level resistant, clinical MRSA strains and *mecA*⁺ *rpoB*^{*} (SJF5003) were grown overnight
136 in the presence of 25 µg ml⁻¹ methicillin (or 50 µg ml⁻¹ where stated), diluted to an initial OD₆₀₀
137 of 0.05, prior to growth to exponential phase (OD₆₀₀ ~0.5) in the presence of 25 µg ml⁻¹
138 methicillin (or 50 µg ml⁻¹ where stated) at all times. This gives a total of over 8 generations in
139 the presence of a high level of methicillin. This concentration of methicillin is sub-MIC for
140 these strains and does not significantly affect growth rate in liquid culture. *mecA*⁺ (SJF4996)
141 was grown in TSB overnight, diluted to an initial OD₆₀₀ of 0.05, prior to growth in the presence
142 of 1.5 µg ml⁻¹ methicillin (sub-MIC) to exponential phase (OD₆₀₀ ~0.5). This concentration of
143 methicillin is sub-MIC for this strain and does not significantly affect growth rate in liquid
144 culture. Finally, SH1000 and *mecA*⁺ (SJF4996) were grown in TSB overnight, diluted to an
145 initial OD₆₀₀ of 0.05, prior to growth to exponential phase (OD₆₀₀ ~0.5), followed by the
146 addition of 1.5 µg ml⁻¹ methicillin (supra- and sub-MIC, respectively) and their phenotype
147 followed over the next 3h.

148 MIC determination and evaluation of MRSA resensitizing compounds

149 Oxacillin MIC values were determined using E-test MIC Evaluator (Liofilchem or bioMérieux)
150 strips in triplicate. MIC values of resensitizing compounds were determined for SH1000 by
151 growth overnight in liquid TSB, for ECg (200 µg ml⁻¹), norgestimate (160 µg ml⁻¹),
152 clomiphene (8 µg ml⁻¹) and spermine (320 µg ml⁻¹). Resensitization of *mecA*⁺ *rpoB*^{*} to
153 oxacillin (from > 256 µg ml⁻¹ (control) to ≤ 4 µg ml⁻¹ (with resensitizer) was determined using
154 ECg (50 µg ml⁻¹), norgestimate (10 µg ml⁻¹), clomiphene (4 µg ml⁻¹) or spermine (202 µg ml⁻¹)
155 in TSA, spread with 200 µl of an overnight culture (diluted normalised to an OD₆₀₀ of ~2 in
156 TSB) and overlaid with an E-test strip. The above resensitizer treatments also led to a drop in
157 oxacillin MIC from > 256 µg ml⁻¹ to ≤ 12 µg ml⁻¹ for the clinical strains (COL, Mu50,
158 MRSA252, TW20, USA300 (HL) and EMRSA15 (HL), apart for TW20 with norgestimate
159 (170 µg ml⁻¹) and clomiphene (42 µg ml⁻¹). The effect of resensitizers on the growth of *S.*
160 *aureus* strains was determined using the above sub-MIC concentration of compounds.

161 Fluorescence microscopy

162 Fixed and labelled cells were dried onto a poly-L-lysine-coated slide, mounted in SlowFade
163 Gold (Thermo Fisher) and imaged using a Nikon Ti inverted microscope fitted with a
164 Lumencor Spectra X light engine. Images were obtained using a 100× PlanApo (1.4 NA) oil
165 objective using 1.518 RI oil and detected by an Andor Zyla sCMOS camera. The raw data in
166 format .nd2 with three channels (ADA-DA, NHS-ester and brightfield) were used for cell
167 volume and PG synthesis analysis.

168 PFA fixation

169 Cells were treated with 1.6% (wt/vol) paraformaldehyde for 30 min at RT and PFA removed
170 by washing cells with water prior to imaging.

171 ADA-DA labelling

172 Cells were incubated with 1 mM ADA-DA (azido-D-alanyl-D-alanine, produced as previously
173 described (8) at 37°C. Cells were washed, fixed with PFA, and labelled with Alexa Fluor 488
174 Alkyne (Merck) (for fluorescent labelling of the ADA-DA azide group) by the click reaction

175 (copper(I)-catalysed alkyne-azide cycloaddition) using the Click-iT™ Cell Reaction Buffer
176 Kit (Invitrogen) according to the manufacturer's instructions.

177 NHS-ester labelling

178 Cells were incubated with 8 µg ml⁻¹ NHS-ester Alexa Fluor 555 in PBS for 5 min on ice. Cells
179 were then washed in ice cold PBS and fixed with PFA.

180 Fluorescence intensity measurements

181 Fluorescence intensity of incorporated ADA-DA clicked to Atto488 was measured using Image
182 J/Fiji and calculated as counts/pixel.

183 Preparation of whole cell lysates

184 Cells resuspended in PBS were lysed using Lysing Matrix B and FastPrep homogeniser (MP
185 biomedical) in 10 cycles of 30 s, at speed of 6.5 m s⁻¹, with a 3-min incubation on ice between
186 cycles. Broken cells were separated from unbroken cells and lysing matrix by centrifugation
187 (5,000 x g, 5 min, 4°C). Total protein concentration was established using the BCA protein kit
188 (Pierce).

189 Western Blot

190 A total of 50 µg protein was separated on a 10% (w/v) SDS-PAGE gel and transferred onto a
191 nitrocellulose membrane. Membranes were blocked in 5% (w/v) skimmed-milk in TBST
192 (20 mM Tris-HCl, pH 7.6; 17 mM NaCl; 0.1% (v/v) Tween-20) and incubated with polyclonal
193 primary antibodies (1:1,000 dilution for anti-PBP1; 1:2,500 dilution for anti-PBP2) overnight
194 at 4°C. For detection, horseradish peroxidase-conjugated goat anti-rabbit IgG (Sigma; 1:10,000
195 dilution) and Clarity Western ECL Substrate (BioRad) were used according to the
196 manufacturer's instructions. Chemiluminescence was detected using Syngene G:BOX Chemi
197 XX9.

198

199 BocillinFL gel-based analysis

200 BocillinFL binding was adapted from a published method (35). Whole cell lysates (50 µg total
201 protein) were incubated with 100 µM BocillinFL (Invitrogen) for 15 min at 30°C. The reaction
202 was stopped by the addition of 5x SDS-PAGE loading buffer and incubation for 15 min at
203 30°C. The proteins were separated on a 10% (w/v) SDS-PAGE gel and visualized using a Bio-
204 Rad ChemiDoc MP imaging system or a GE Typhoon FLA 9500.

205 Transmission electron microscopy (TEM)

206 Cell preparation for electron microscopy was performed as described previously (15). Cell
207 pellets (5 ml cultures) were fixed overnight at 4°C in 2.5% (w/v) EM grade glutaraldehyde
208 (Agar Scientific). Samples were washed with PBS and resuspended in 2% (w/v) aqueous
209 osmium tetroxide (Agar Scientific) for secondary fixation (2 h at room temperature). Cells were
210 washed with PBS and dehydrated by incubating with increasing concentrations of ethanol (60,
211 75, 95 and 100% (v/v) ethanol) 15 min each. Ethanol was removed and samples were incubated
212 with propylene oxide (Agar Scientific) to complete dehydration. Samples were mixed with a

213 1:1 mix of propylene oxide and Epon resin (Agar Scientific) and incubated overnight at room
214 temperature to allow infiltration. The majority of the resin was removed, and the excess of
215 propylene oxide evaporated at room temperature. Two consecutive incubations of the samples
216 with pure Epon resin (4 h each) were performed and cells were embedded in fresh resin. Resin
217 polymerisation was achieved by incubation at 60°C for 48 h. Thin sections (85 nm) were
218 produced using an Ultracut E Ultramicrotome (Reichert-Jung) and mounted onto 300-square
219 mesh nickel TEM grids (Agar Scientific). Sections were stained in 3% (w/v) aqueous uranyl
220 acetate (Polysciences Inc., 21447) for 25 min, washed with dH₂O and stained with Reynold's
221 lead citrate for 5 min. The citrate was removed by washing with dH₂O. A FEI Tecnai T12 Spirit
222 Transmission Electron Microscope operating at 80 kV was used for imaging. A Gatan Orius
223 SC1000B bottom-mounted CCD camera recorded the images. EM images were analysed using
224 Fiji (42). Over 300 cells were counted for each repeat, with at least two independent repeats
225 per sample/treatment. Cells were categorised according to their phenotypic features as normal
226 and abnormal, dependent on septal misplacement or growth defects.

227 Extraction and purification of PG

228 PG was extracted as previously described (16). Briefly, cells were grown in the presence or
229 absence of IPTG for 2-4 h for PBP1 and PBP2 depletion experiments or to mid-exponential
230 phase with or without methicillin for methicillin-treatment experiments and boiled at 100°C
231 for 15 min to kill the cells. Boiled cells were recovered by centrifugation at 20,000 x g for 3
232 min and the supernatant was discarded. Next, the pellets were suspended in PBS and transferred
233 to the lysing matrix tubes containing 0.1 mm silica beads and broken using FastPrep 24
234 Homogeniser (10 cycles of 30 s, at speed of 6.5 m s⁻¹, with a 3-min incubation on ice between
235 cycles). Next, the tubes were centrifuged at 170 x g at RT to remove the beads and the
236 supernatant, containing the broken cells, was pipetted into new Eppendorf tubes, which were
237 then centrifuged at 20,000 x g at RT for 3 min. PG was resuspended in 5% (w/v) SDS solution
238 and boiled at 100°C for 25 min. Boiling in SDS was repeated one more time for 15 min and
239 the PG was serially rinsed with Milli-Q water. Lastly, PG was resuspended in a solution of 50
240 mM Tris HCl pH 7, containing 2 mg ml⁻¹ of pronase, and incubated at 60°C for 90 min.
241 Afterwards, PG was rinsed thrice with HPLC grade water, and stored at 4°C without any further
242 treatment.

243 PG immobilisation and AFM imaging

244 To immobilise purified PG, a mica substrate was coated with Cell-tak (Corning, Netherlands),
245 which is a solution of polyphenolic proteins. Briefly, the mica substrate was incubated with
246 180 µl of Cell-tak solution (171 µl of 100 mM sodium bicarbonate (NaHCO₃) pH 8.0, 3 µl of
247 1 M sodium hydroxide (NaOH), and 6 µl of 1.05 mg ml⁻¹ Cell-tak) for 30 min. Next, the
248 substrate was rinsed three times with HPLC grade water and then dried with nitrogen flow.
249 Fifty microliters of diluted PG solution was then added to the Cell-tak coated substrate,
250 incubated for 1 h and rinsed with HPLC grade water and dried with nitrogen flow. For thickness
251 measurements, AFM height topographic images of dehydrated PG were captured in air using
252 AFM tapping mode with Nunano SCOUT 350 - Silicon AFM probe (spring constant: 42 N/m,
253 Resonance frequency: 350 kHz) at free amplitude of 10 nm with set point of 70-80% of free
254 amplitude (e.g. 7 nm) on a Dimension FastScan Bio (Bruker, Santa Barbara). For AFM high-
255 resolution imaging, all the high-resolution images were acquired in Peak force tapping mode
256 in imaging buffer (10 mM Tris; 200 mM KCl; 10 mM MgCl₂, pH 8.0) with the Bruker
257 Fastscan-D cantilevers at the range of 1-3 nN peak force set point on a Dimension FastScan
258 AFM (Bruker, Santa Barbara). The imaging parameters used are as follows; Scan rate: 1 Hz;
259 Scan angle: 0°; Peak Force frequency: 2-8 kHz, Peak force amplitude: 80-100 nm, and with

260 high pixel resolution. Prior to high-resolution imaging, the spring constant and deflection
261 sensitivity of the cantilevers were calculated using the Sader thermal spectra method.

262 PG thickness measurement data processing

263 To manually measure the thickness of AFM topographic height images of dehydrated PG were
264 imported into Gwyddion 2.55, masked and levelled using first order polynomial row fit. The
265 thickness of the single leaflet of the PG was measured using the one-dimensional statistical
266 function tool, which computes the average height density across the image frame (or selected
267 area). The height density graph was plotted with their characteristic two peaks. Then, Gaussian
268 functions were fitted on each peak and the background peak was subtracted from the peak of
269 the non-background, to give the average height/thickness of the PG fragment.

270 AFM three-dimension (3D) image processing

271 The pseudo 3D AFM images in Fig. 1Aii-Eii, Fig. 2Eii (+ IPTG, -IPTG), and Fig. 3Eii-Fii,
272 were processed using Nanoscope analysis software. The following image processing
273 parameters were used; Pitch = 10, Z-axis aspect ratio = 0.3, image rotation = 0°, plot type =
274 height, and projection = parallel.

275 Fibre detection and orientation quantification

276 Peptidoglycan fibres in AFM images were detected and quantified using automated image
277 analysis methods. Our framework was implemented as a Matlab GUI, which accepts outputs
278 from Gwyddion or open-source alternatives such as TopoStats (43). In the first stage, we
279 upsampled all images to a uniform resolution (0.1 nm/pixel) to ensure uniformity of analyses
280 across samples. Flattening using a Difference of Gaussians (DoG) filter removed low spatial-
281 frequency components, separating the high spatial-frequency PG fibre network from the overall
282 geometry of the cell wall. Individual PG fibres were segmented by employing a ridge-detection
283 algorithm (44), the results of which were then fused into a continuous network using a
284 Watershed algorithm (45) to remove small gaps between fibres at crossing points. This rough
285 network was then skeletonised and converted to a graph consisting of nodes, representing fibre-
286 fibre crossing points, linked by edges, representing fibre bodies. This graph-based network was
287 then cleaned based on its topology, removing disconnected fibre sections and fusing adjacent
288 T-shaped configurations of fibres to more accurately capture X-shaped fibre-fibre crossings.
289 Edges and nodes were then assigned to separate fibres based on the original segmentation of
290 the fibre network. Finally, we measured the local orientation of fibres by considering each point
291 along the length of the fibre in turn, performing a linear regression on the points assigned to
292 the fibre within a neighbourhood of 10 pixels of the query point and used the resulting
293 regression slope as the orientation measurement. From these local orientation measurements,
294 we computed the angular histogram for each image. The fibreFinder codes are publicly
295 available (46).

296 Pore analysis and quantification using Fiji

297 To calculate the area of the pores distributed across both the inner and outer section of the PG,
298 we used a custom-made semi-automated pore analysis macro (AFM_Slicer) in an open-source
299 software ImageJ/FIJI (42). Firstly, the macro pre-filtered the high-resolution image by
300 downscaling the pixel number and removing the noise of the image using the despeckle tool in
301 FIJI. Next, the treated image was simultaneously binarized and sliced into stacks of binary
302 slices where black represented the fibres in the image and white denoted the pores. Lastly, the
303 area of the pores in each slice was calculated using the analyze particle tool, followed by

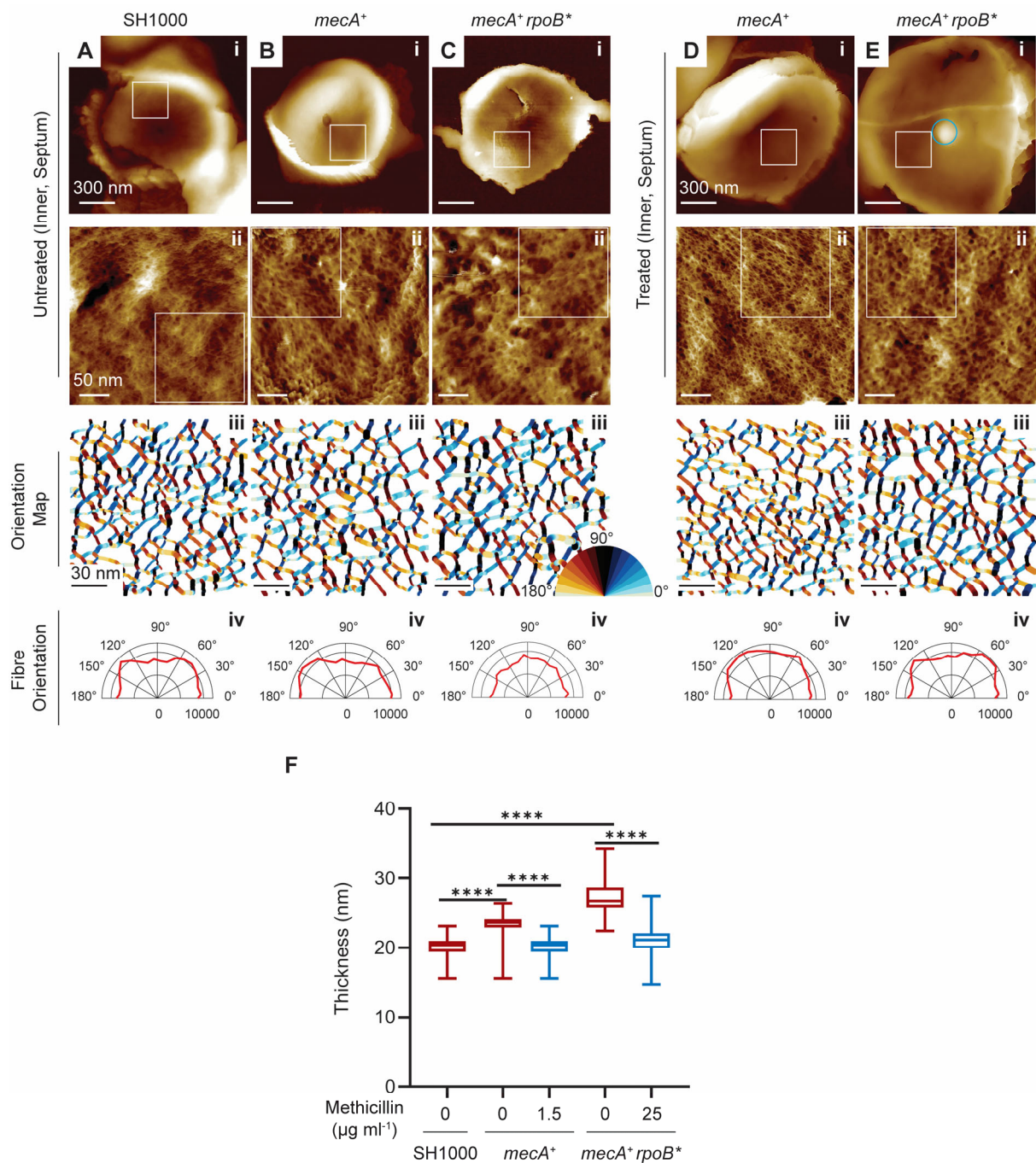
304 calculation of the cumulative fraction of the pore area in each slice. The slice for each image
305 that had the maximum number of pores was used for the graphs in figs. S2, S6 and S10 (47).

306 Measurement of (p)ppGpp levels

307 *S. aureus* strains were grown overnight in low-phosphate CDM (39) at 37°C. Cultures were
308 diluted to an OD₆₀₀ of 0.1 and grown for 2.5 h prior to the addition of 3.7 MBq of [³²P]H₃PO₄
309 and incubation for a further 3 h at 37°C. Cultures were subsequently normalized for optical
310 density, cells recovered by centrifugation (17,000 × g for 5 min) and suspended in 100 µl of
311 600 mM formic acid. Cells were subjected to three freeze/thaw cycles and debris removed by
312 centrifugation (17,000 × g for 5 min) before the lysate was filtered through a 3 kDa spin
313 column. Ten microliters were subsequently spotted on PEI-cellulose F thin-layer
314 chromatography (TLC) plates (Merck Millipore), nucleotides separated, and TLC plates
315 developed using a 1.5 M KH₂PO₄, pH 3.6, buffer. The radioactive spots were visualized using
316 an FLA 7000 Typhoon PhosphorImager, and data were quantified using ImageQuantTL
317 software.

318 Cell volume measurements

319 The cell volume measurements from the microscopy images were performed using a semi-
320 automatic analysis approach (CocciVol) with a combination of FIJI macros (available at
321 <https://github.com/Laia-Pasquina/CocciVol>) and a user-friendly machine learning interactive
322 open-source software named ilastik (48). First the raw data from the confocal Nikon
323 microscope was obtained in a file format .nd2. The raw data contains a stack of 11 slices across
324 3 µm with the cells focused approximately on the middle with a minimum of three channels:
325 ADA-DA, NHS-ester and brightfield. The *Macro1_V2_Filtering_preparing_image.ijm* file in
326 GitHub opens the raw image and creates a Z stack from the NHS-ester channel of 3 slices
327 around the focus (which needs to be pre-determined by the user by opening the image with FIJI
328 and manually finding the focus). Then, the image in .png format is processed in ilastik using
329 two projects. The first ilastik project uses machine learning to run a pixel segmentation routine
330 to learn from the users input in a few cells and then classify the rest of the cells in what pixels
331 correspond to cells and what pixels are background. The second ilastik project uses an object
332 classification routine similar to the first one but that classifies the cells into good fit or bad fit
333 for volume analysis as well as applying some watershed filters to distinguish cells that are too
334 close together (like diploids). Finally, the ilastik program outputs a table with the analysis of
335 several physical parameters for each cell, which requires further processing to obtain the
336 volume of the cells. This additional processing is carried out with
337 *Macro2_Calculate_Volume_from_table.ijm* in FIJI (42) to obtain an Excel table with each cell
338 number, volume and the ratio between the short axis and the long axis of the cell. Once one
339 image was analysed for one type of sample there is a batch processing option in ilastik which
340 was used to process an average of 5 images per sample. Using this approach, n = 600 images
341 can be analysed in 30 min or less and a similar number of cells were analysed for each sample.
342 Several samples were compared to each other in this manuscript. The CocciVol approach was
343 used for the graphs in figs. S4, S5 & S9 (49).

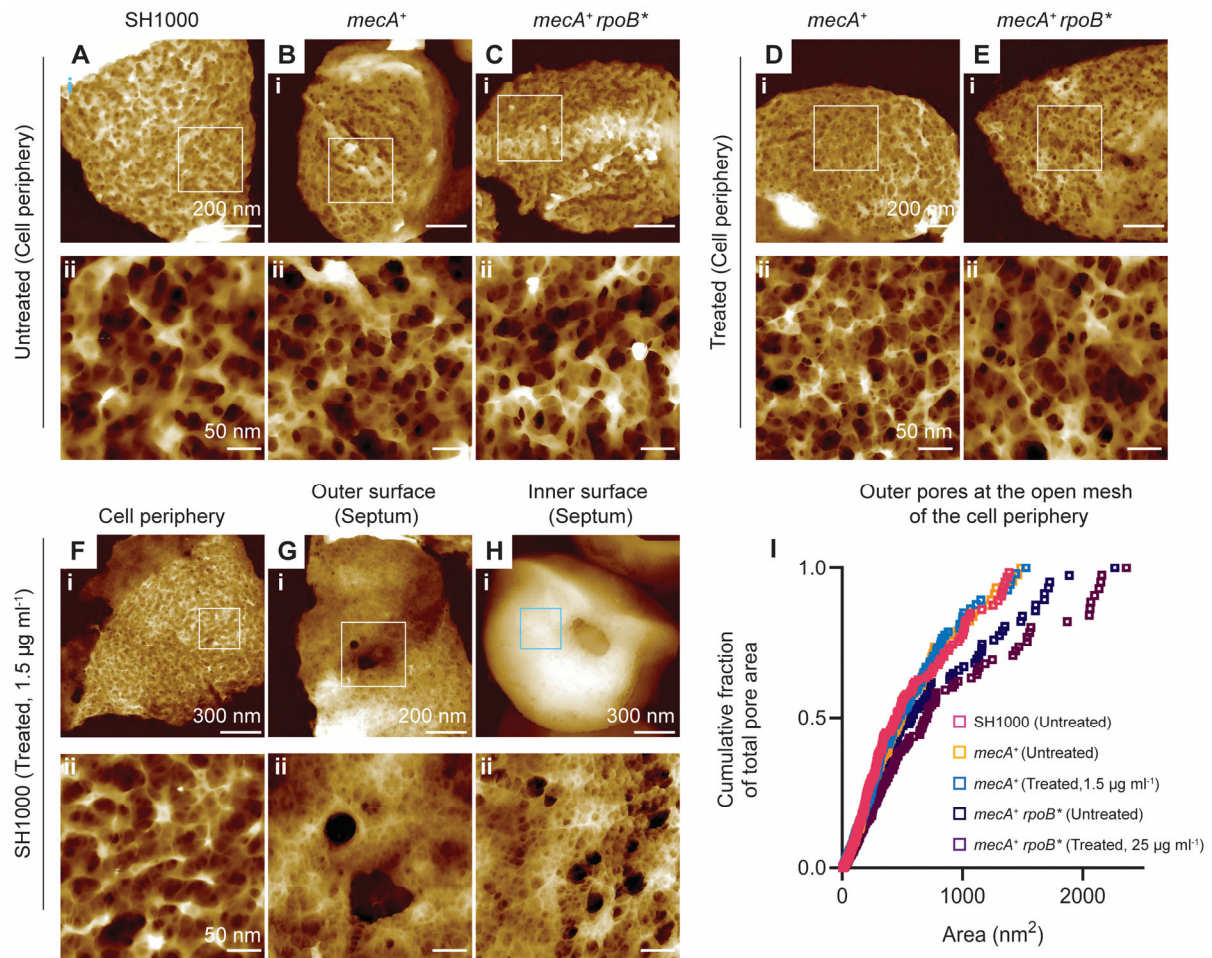


344

345 **Fig. S1.**

346 Effect of methicillin on the PG architecture of the inner surface of the septum in MRSA. (A-
 347 F) Parental MSSA strain, SH1000 (A) and MRSA strains, *mecA*⁺ (B, D) and *mecA*⁺ *rpoB*^{*} (C,
 348 E) were grown without (Untreated; A-C) or with methicillin (Treated; D, E), at 1.5 and 25 µg
 349 ml⁻¹ for D and E respectively. (i) AFM images of the inner surface of the septum and (ii)
 350 corresponding higher resolution topographic images of the selected location marked with white
 351 square in (i). The topographical height (z) range is as follows; (Ai) 230 nm, (Aii) 13 nm, (Bi)
 352 420 nm, (Bii) 11 nm, (Ci) 170 nm, (Cii) 13.5 nm, (Di) 545 nm, (Dii) 11.5 nm, (Ei) 520 nm,
 353 (Eii) 8 nm. The circle in (E) indicates the presence of a cell wall lump which is a characteristic
 354 feature of *mecA*⁺ *rpoB*^{*} when treated with methicillin. The minimum height of the lump is 10
 355 nm (n = 10, hydrated sacculi). (iii) Represents the colour-coded orientation map of the fibre

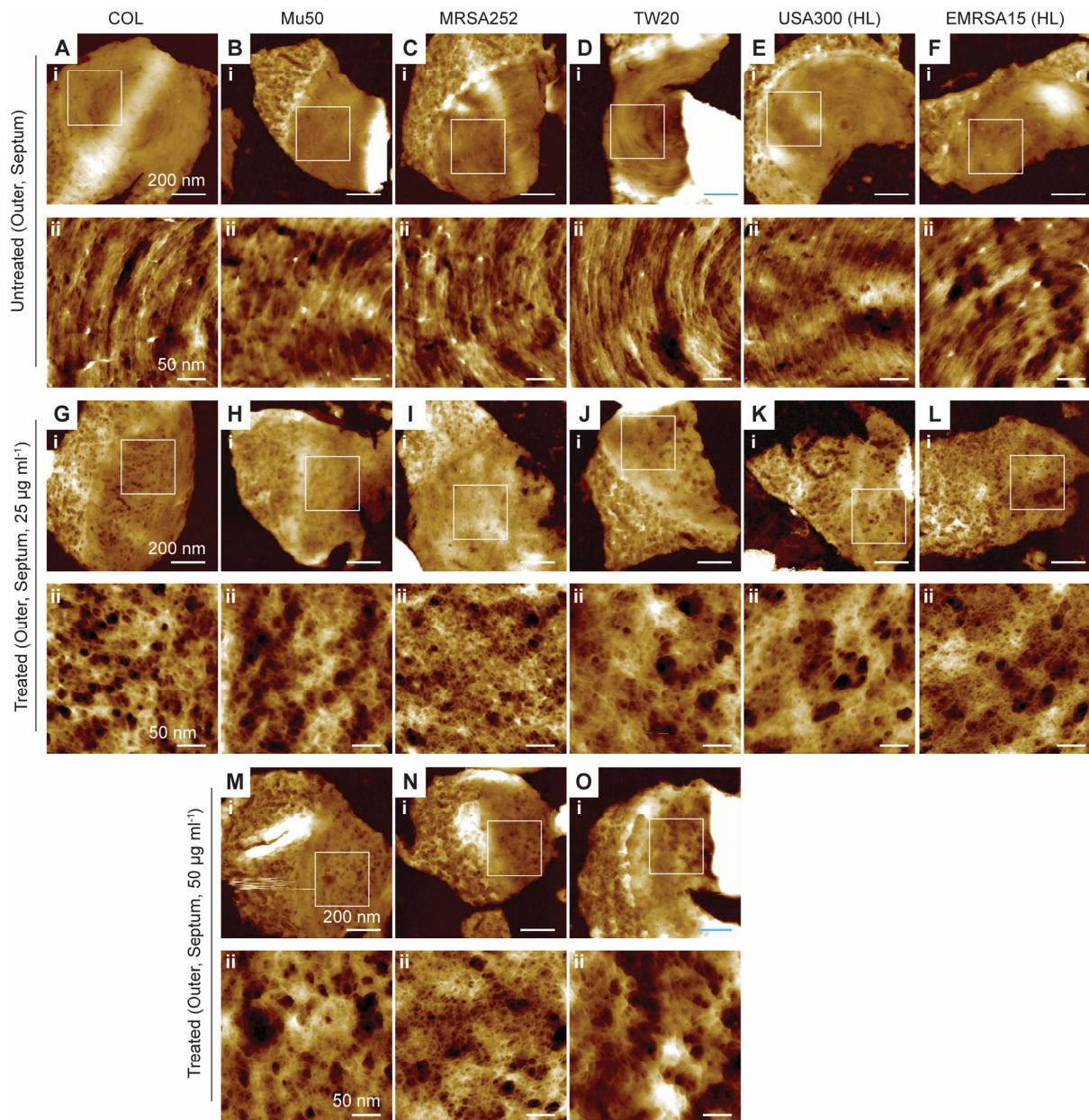
356 chains detected within the white box in (ii), and (iv) depicts the angular histogram of combined
357 orientation of three independent AFM images. The image analysis method used for glycan
358 orientation detection is described in the Materials and Methods section. (F) Plot of the
359 measured thickness of dehydrated sacculi of SH1000, *mecA*⁺ and *mecA*⁺ *rpoB*^{*} with respect to
360 without (red) and with methicillin treatment (light blue). The thickness data were compared
361 using the Mann-Whitney test (****, $P < 0.0001$, $n = 28$ for each strain and condition). Data are
362 representative of three independent biological repeats.



363

364 **Fig. S2.**

365 Effect of methicillin on the PG architecture of the cell periphery of MRSA strains. (A-C) The
 366 parental MSSA strain, SH1000 ((A) and MRSA strains, *mecA*⁺ (B) and *mecA*⁺ *rpoB*^{*} (C) were
 367 grown without (Untreated; A-C) or with methicillin (Treated; D, E), at 1.5 and 25 μg ml⁻¹ for
 368 D and E, respectively. (i) AFM images of the outer open mesh of the cell wall periphery and
 369 (ii) corresponding higher resolution topographic images of the selected location marked with
 370 white square in (i). The topographical height (z) range is as follows; (Ai) 80 nm, (Aii) 33 nm,
 371 (Bi) 110 nm, (Bii) 45 nm, (Ci) 140 nm, (Cii) 48 nm, (Di) 100, (Dii) 35 nm, (Ei) 95 nm, (Eii)
 372 45 nm. (F-H) AFM images of (i), low resolution and (ii) corresponding higher resolution
 373 topographic images of the selected location marked with white square in (i) of sacculi of
 374 SH1000 treated 1.5 μg ml⁻¹ methicillin. (F) Outer PG mesh at the cell periphery; (G) Outer
 375 surface of the septum; (H) Inner surface of the septum. The topographical height (z) range is
 376 as follows; (Fi) 70 nm, (Fii) 35 nm, (Gi) 95 nm, (Gii) 43 nm, (Hi) 950 nm, (Hii) 48 nm. (I)
 377 Combined plot of cumulative fraction of total pore area, distributed over the outer open mesh
 378 shown in (A-E) (ii). Data are representative of three independent biological repeats and five
 379 AFM-independent images.

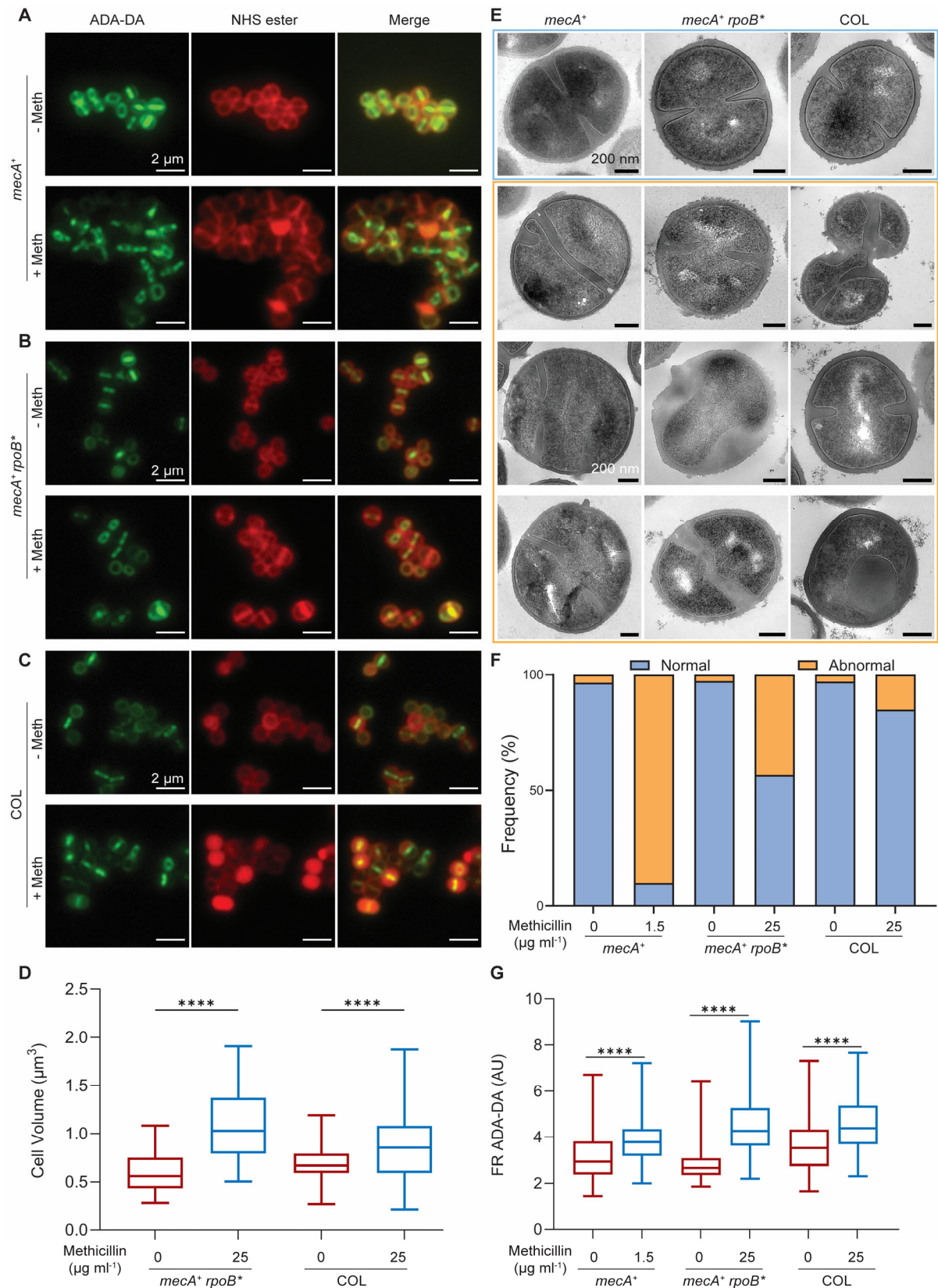


380

381 **Fig. S3.**

382 AFM characterization of high level resistant clinical strains. (A-F) Show AFM topographic
 383 images of the outer surfaces of newly revealed septa in samples of isolated sacculi of untreated
 384 (A) COL, (B) Mu50, (C) MRSA252, (D) TW20, (E) USA300(HL), and (E) EMRSA15(HL).
 385 (i) Low-resolution AFM images and (ii) corresponding higher-resolution images of the region
 386 indicated by the white boxes in (i). The topographical height (z) range is as follows; (Ai) 150
 387 nm, (Aii) 13.5 nm, (Bi) 85 nm, (Bii) 11 nm, (Ci) 75 nm, (Cii) 9 nm, (Di) 65 nm, (Dii) 11.5 nm,
 388 (Ei) 80 nm, (Eii) 13.5 nm, (Fi) 105 nm, and (Fii) 11.5 nm. (G-L) Show outer surfaces of the
 389 septa of the same strains treated with 25 $\mu\text{g ml}^{-1}$ methicillin. (i) Low-resolution AFM images
 390 and (ii) corresponding higher-resolution images of the region indicated by the white boxes in
 391 (i). The topographical height (z) range is as follows; (Gi) 95 nm, (Gii) 16 nm, (Hi) 90 nm, (Hii)
 392 18 nm, (Ii) 65 nm, (Iii) 12 nm, (Ji) 88 nm, (Jii) 24 nm, (Ki) 60 nm, (Kii) 25 nm, (Li) 65 nm,
 393 and (Lii) 35 nm. (M-O) Show the outer surface of the newly revealed septa of Mu50,
 394 MRSA252, and TW20 treated with 50 $\mu\text{g ml}^{-1}$ methicillin. (i) Low-resolution AFM images and
 395 (ii) corresponding higher-resolution images of the region indicated by the white boxes in (i).

396 The topographical height (z) range is as follows; (Mi) 130 nm, (Mii) 36 nm, (Ni) 105 nm, (Nii)
397 24 nm, (Oi) 78 nm, and (Oii) 28 nm. Data are representative of two independent biological
398 repeats and three AFM-independent images.

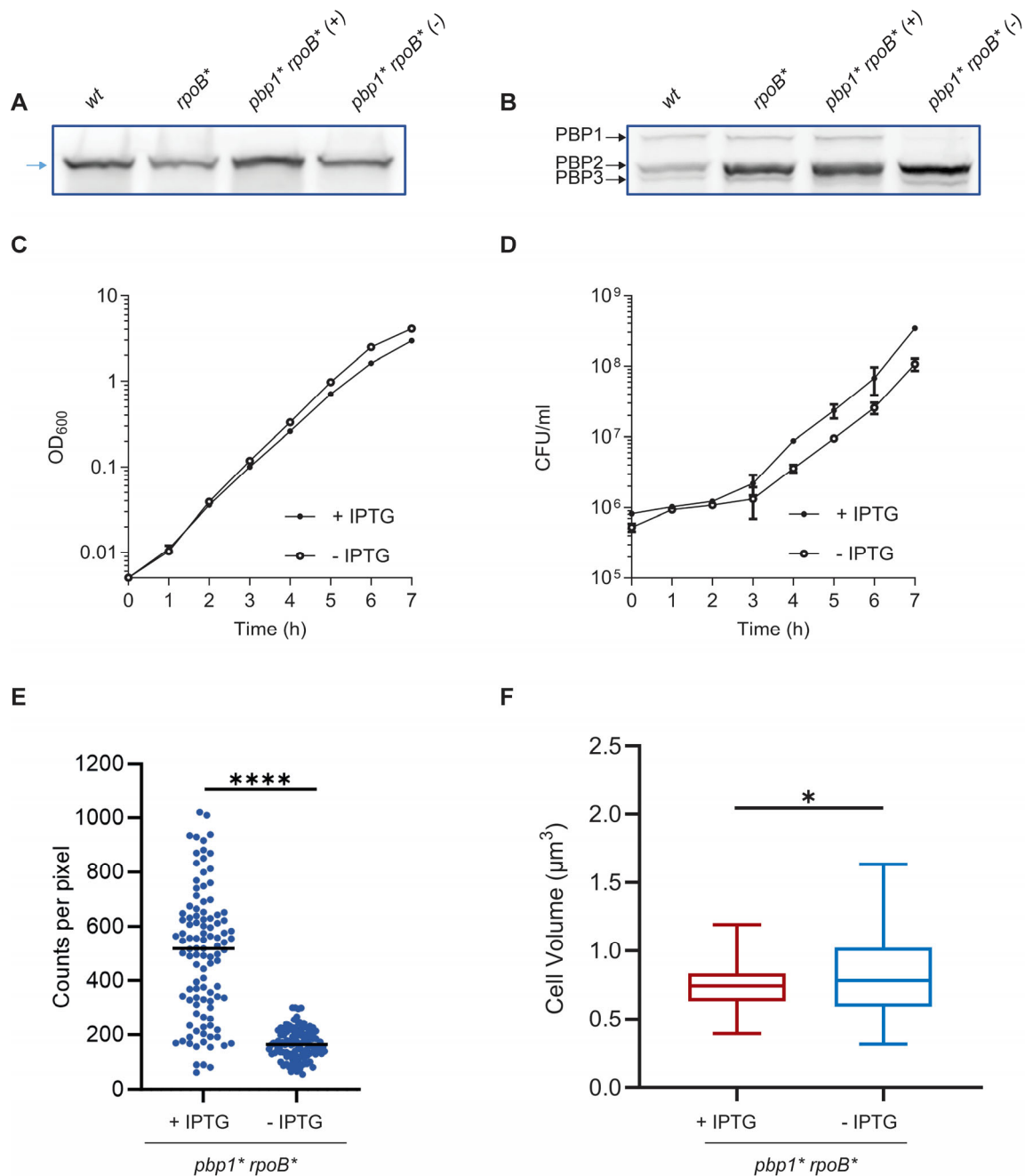


399

400 **Fig. S4.**

401 Effect of methicillin on cell morphology of MRSA strains. (A-C) Fluorescence microscopy
 402 images of ADA-DA and NHS-ester labelled MRSA strains (A) *mecA*⁺, (B) *mecA*⁺ *rpoB*^{*}, and
 403 (C) COL grown without (-Meth, i) or with methicillin (+Meth, ii), at 1.5, 25 and 25 $\mu\text{g ml}^{-1}$

404 for **A**, **B** and **C**, respectively. **(D)** Cell volumes of *mecA*⁺ *rpoB** and COL without and with
405 methicillin (1.5 µg ml⁻¹ and 25 µg ml⁻¹), as measured by fluorescence microscopy after NHS-
406 ester Alexa Fluor 555 labelling. The *P* value was determined by Mann-Whitney U tests (****,
407 *P* < 0.0001). The number of cells analysed per sample was n ≥ 300. **(E)** Shows TEM images of
408 *mecA*⁺, *mecA*⁺ *rpoB** and COL grown with methicillin at 1.5, 25 and 25 µg ml⁻¹ respectively.
409 Representatives of cells with normal septa are within a light blue frame while cells with
410 abnormal septa are within orange frame. **(F)** Quantification of cellular phenotypes based on
411 TEM. Cells were categorised as normal and abnormal, depending on the presence of a
412 misplaced, multiple or misshapen septa or other cell cycle defects. Scale bar = 200 nm. Data
413 are representative of two independent biological repeats (n ≥ 300). **(G)** Fluorescence ratio (FR)
414 was calculated by dividing the fluorescence intensity at the septum by the intensity at the cell
415 periphery of *mecA*⁺, *mecA*⁺ *rpoB**, and COL grown without (red, 0 µg ml⁻¹) and with
416 methicillin (light blue) at different concentrations 1.5, 25 and 25 µg ml⁻¹ respectively.
417 Differences are highly significant (*****P* < 0.0001) with higher FR for cells treated with
418 methicillin (light blue) compared to no treatment (red). Higher values indicate more PG
419 incorporation at the septum whilst lower values mean more peripheral PG. Number of cells
420 analysed for each sample was 100.

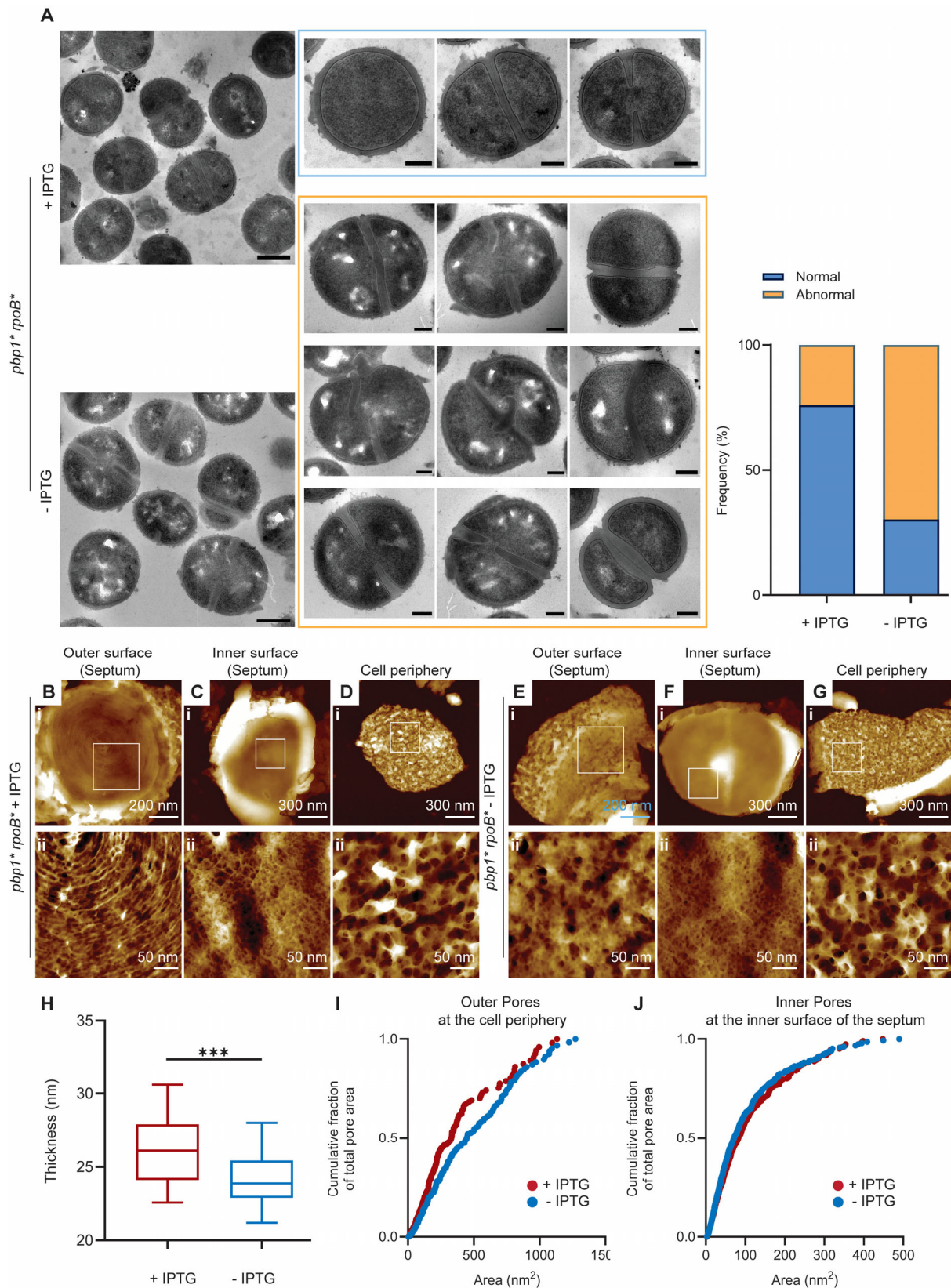


421

422 **Fig. S5.**

423 Analysis of the role of PBP1 transpeptidase activity. (A) Immunoblot of whole cell lysates of
 424 SH1000, *rpoB** and *pbp1* rpoB** grown with IPTG (+) without IPTG (-) for 4 h analysed using
 425 anti-PBP1 antibody. Expected PBP1 and PBP1* size = 83 kDa (blue arrowhead). (B)
 426 BocillinFL gel-based analysis of PBPs in SH1000, *rpoB** and *pbp1* rpoB** grown with IPTG
 427 (+) without IPTG (-) for 4 h; the locations of PBPs on the blots are indicated (arrows). (C)
 428 Growth curves of *pbp1* rpoB** grown in the presence or absence of IPTG (+ IPTG and - IPTG,
 429 respectively). Data represent the mean ± SD. Error bars that are smaller than the data point
 430 symbols are not shown. (D) CFU counts of *pbp1* rpoB** grown in the presence or absence of
 431 IPTG (+ IPTG and - IPTG, respectively). Data represent the mean ± SD. Error bars that are
 432 smaller than the data point symbols are not shown. (E) ADA-DA, clicked to Atto488,
 433 incorporation over 5 min in *pbp1* rpoB** (SJF5306) grown with IPTG (+) and without IPTG
 434 (-). Fluorescence intensities were compared using a one-way ANOVA with Tukey's multiple

435 comparison test (****, $P < 0.0001$). Number of cells analysed for each sample was $n = 110$.
436 Each dot represents a single cell. A black line indicates the median of each distribution. Data
437 are representative of three independent biological repeats. (F) Cell volumes of *pbp1* rpoB**
438 after incubation with (+, red, average cell volume is $0.75 \pm 0.16 \mu\text{m}^3$) or without (-, light blue,
439 average cell volume is $0.83 \pm 0.30 \mu\text{m}^3$) IPTG for 4h, as measured by fluorescence microscopy
440 after NHS-ester Alexa Fluor 555 labelling. The P value was determined by Mann-Whitney U
441 tests (*, $P = 0.0266$). Number of cells analysed for each sample was ≥ 250 .

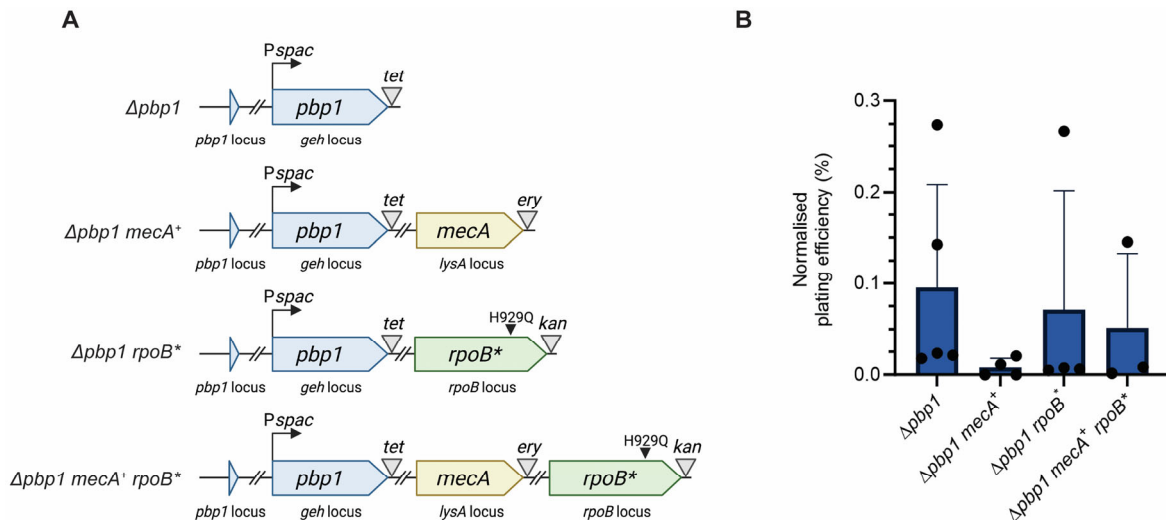


442

443 **Fig. S6.**

444 Cell wall morphology of *pbp1* rpoB** revealed by TEM and AFM. (A) Left, representative
 445 TEM micrographs of *pbp1* rpoB** grown for 4 h in the presence and absence of IPTG. Scale
 446 bars = 500 nm. Examples of cells classified as normal and abnormal phenotypes are shown

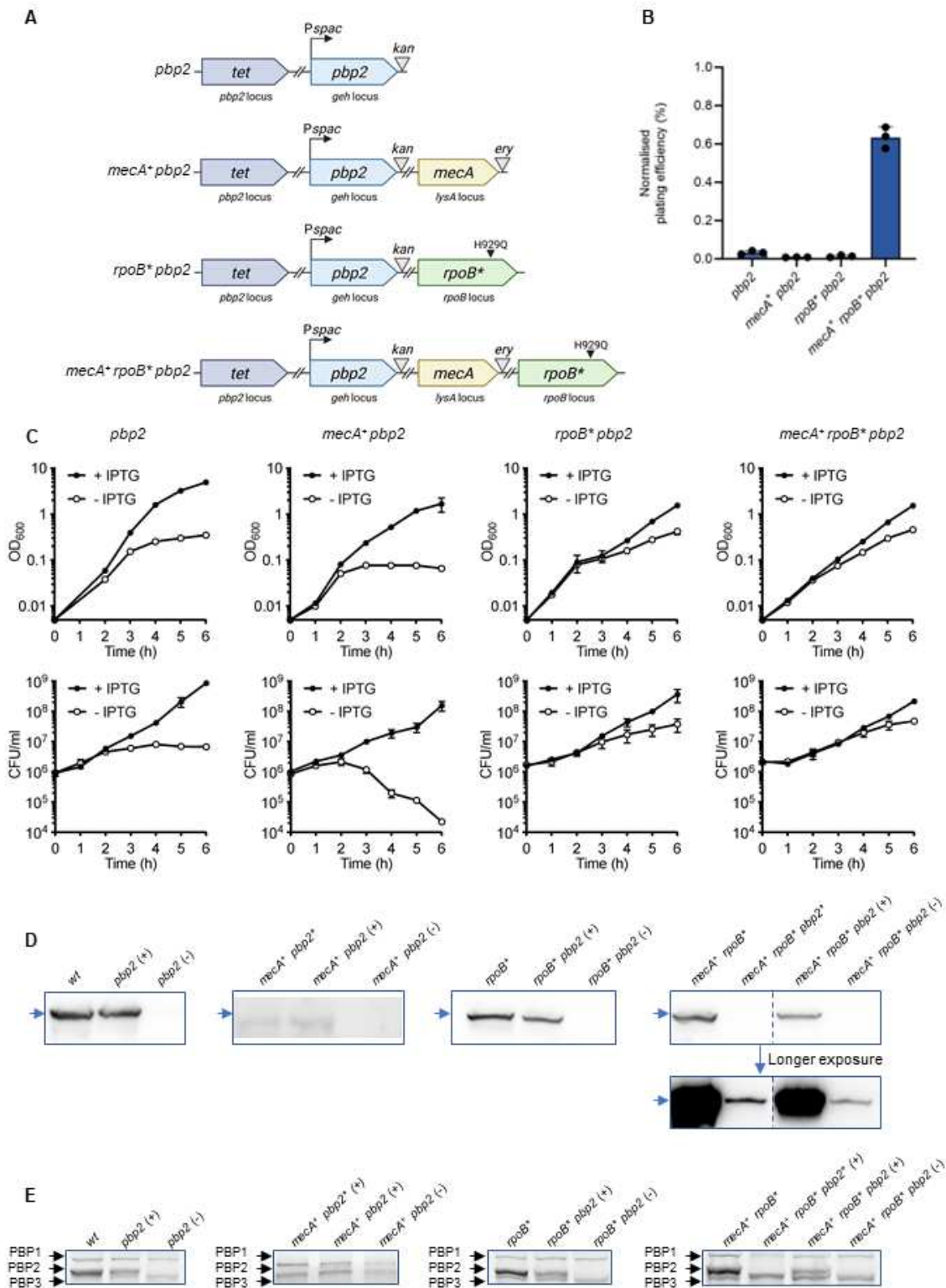
447 within the light blue (+IPTG) and orange frames (-IPTG), respectively. Scale bar = 200 nm.
448 TEM data are representative of two independent biological repeats with $n \geq 300$ per
449 sample. Right, quantification of cellular phenotypes associated with *pbpl* rpoB**, based on
450 the TEM data. **(B-G)** AFM images of the outer surface of the septum **(B, E)**, the inner surface
451 of the septum **(C, F)**, and the open mesh at the cell periphery **(D, G)** associated with *pbpl**
452 *rpoB** grown in the presence of IPTG (+ IPTG; **B-D**) and absence of IPTG (- IPTG; **E-G**). For
453 **(B-G)** (i) are individual fragments of sacculus and (ii) are higher resolution topographic AFM
454 images of the selected location marked with the white square in (i). The topographical height
455 (z) range is as follows; + IPTG: 120 nm **(Bi)**, 8.5 nm **(Bii)**, 270 nm **(Ci)**, 13 nm **(Cii)**, 120 nm
456 **(Di)**, 55 nm **(Dii)**. -IPTG: 110 nm **(Ei)**, 22 nm **(Eii)**, 290 nm **(Fi)**, 17 nm **(Fii)**, 120 nm **(Gi)**, 48
457 nm **(Gii)**. Data are representative of three independent biological repeats and more than 10
458 AFM independent imaging experiments. **(H)** Plot of the measured thickness of dehydrated
459 sacculi of *ppbpl* rpoB** after incubation with (+, red) or without (-, light blue) IPTG for 4h.
460 The number of independent fragments measured for each strain was 20. The *P* value was
461 determined by Mann-Whitney U tests (***, $P = 0.0009$). **(I-J)** Cumulative fraction of total pore
462 area as a function of the area of the pores distributed across the open mesh surface of the cell
463 wall periphery surface **(I)** and the inner surface **(J)** of the septum of *pbpl* rpoB** grown in the
464 presence of IPTG (+ IPTG, red) and absence of IPTG (- IPTG, light blue).



465

466 **Fig. S7.**

467 Analysis of the role of PBP1 in growth. (A) Schematic representation of the $\Delta pbb1$ genetic
 468 constructs. An ectopic copy of *pbb1* was placed under the control of the *Pspac* promoter at the
 469 lipase (*geh*) locus, while the gene in the native *pbb1* locus was deleted ($\Delta pbb1$). In $\Delta pbb1$
 470 *mecA*⁺ and $\Delta pbb1 mecA⁺ a copy of a *mecA*⁺ gene under the control of its native promoter
 471 is placed at the *lysA* locus. In $\Delta pbb1 rpoB^*$ and $\Delta pbb1 mecA⁺ *rpoB*[*], the *rpoB* gene has a point
 472 mutation which results in a single amino acid replacement (H929Q) in RNA polymerase β
 473 subunit (*rpoB*[*]). *tet*, *ery* and *kan* represent tetracycline, erythromycin and kanamycin
 474 resistance cassettes, respectively. The graphics were created with BioRender.com. (B) Plating
 475 efficiency of the SH1000 derivatives $\Delta pbb1$, $\Delta pbb1 mecA⁺, $\Delta pbb1 rpoB^*$ and $\Delta pbb1 mecA⁺
 476 *rpoB*[*] in the absence of IPTG. Plating efficiency values were compared with the control groups
 477 grown in the presence of IPTG. Data were compared using a one-way ANOVA with Dunnett's
 478 multiple comparison test (ns, not significant, $P \geq 0.05$, $n \geq 3$). Data represent the mean \pm SD.$$$$

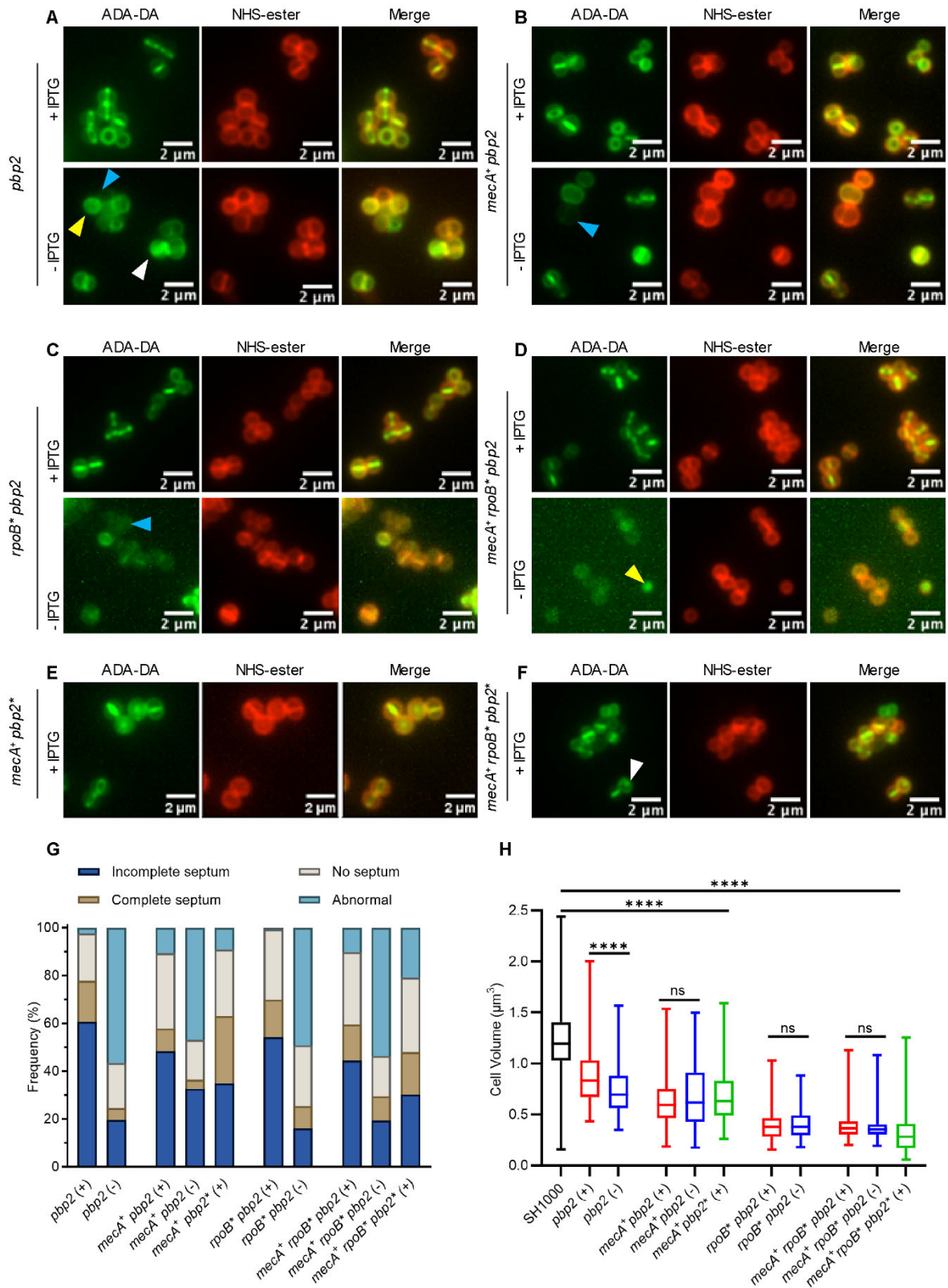


479

480 **Fig. S8.**

481 Analysis of the role of PBP2 in growth. (A) Schematic representation of the *pbp2* genetic
 482 constructs. An ectopic copy of *pbp2* was placed under the control of the Pspac promoter at the
 483 SH1000 lipase (*geh*) locus, while the gene in the native *pbp2* locus was deleted (marked with
 484 *tet*). In *mecA*⁺ *pbp2* and *mecA*⁺ *rpoB*^{*} *pbp2* a copy of a *mecA* gene expressed from its native

485 promoter was located at the *lysA* locus. In *rpoB** *pbp2* and *mecA⁺ rpoB* pbp2* the *rpoB* gene
486 has a point mutation which results in a single amino acid change (H929Q) in the RNA
487 polymerase β subunit (*rpoB**). The graphics were created with BioRender.com. **(B)** Plating
488 efficiency of the derivatives *pbp2*, *mecA⁺ pbp2*, *rpoB* pbp2* and *mecA⁺ rpoB* pbp2* grown in
489 the absence of IPTG. Plating efficiency values were compared with the control groups grown
490 in the presence of IPTG. Data represent the mean \pm SD. **(C)** Growth curves of SH1000
491 derivatives *pbp2*, *mecA⁺ pbp2*, *rpoB* pbp2*, and *mecA⁺ rpoB* pbp2* grown in the presence or
492 absence of IPTG (+ IPTG and - IPTG, respectively). Data represent the mean \pm SD. Error bars
493 that are smaller than the data point symbols are not shown. **(D)** Immunoblots, analysed using
494 anti-PBP2 antibody, of whole cell lysates of SH1000 (wt) and *mecA⁺ rpoB**, *rpoB**, *pbp2*,
495 *mecA⁺ pbp2*, *rpoB* pbp2* and *mecA⁺ rpoB* pbp2* derivatives grown in the presence (+) or
496 absence (-) of IPTG for 4 h. *mecA⁺ pbp2** and *mecA⁺ rpoB* pbp2** were grown in the presence
497 of IPTG throughout. Expected PBP2 and PBP2* sizes = 80 kDa are indicated (blue arrowhead).
498 **(E)** BocillinFL gel-based analysis of PBPs in SH1000 and *mecA⁺ rpoB**, *rpoB**, *pbp2*, *mecA⁺*
499 *pbp2*, *rpoB* pbp2*, and *mecA⁺ rpoB* pbp2* grown in the presence (+) or absence (-) of IPTG
500 for 4 h. *mecA⁺ pbp2** and *mecA⁺ rpoB* pbp2** were grown in the presence of IPTG throughout.
501 Data are representative of two **(D and E)** and three **(B and C)** independent biological
502 experiments.

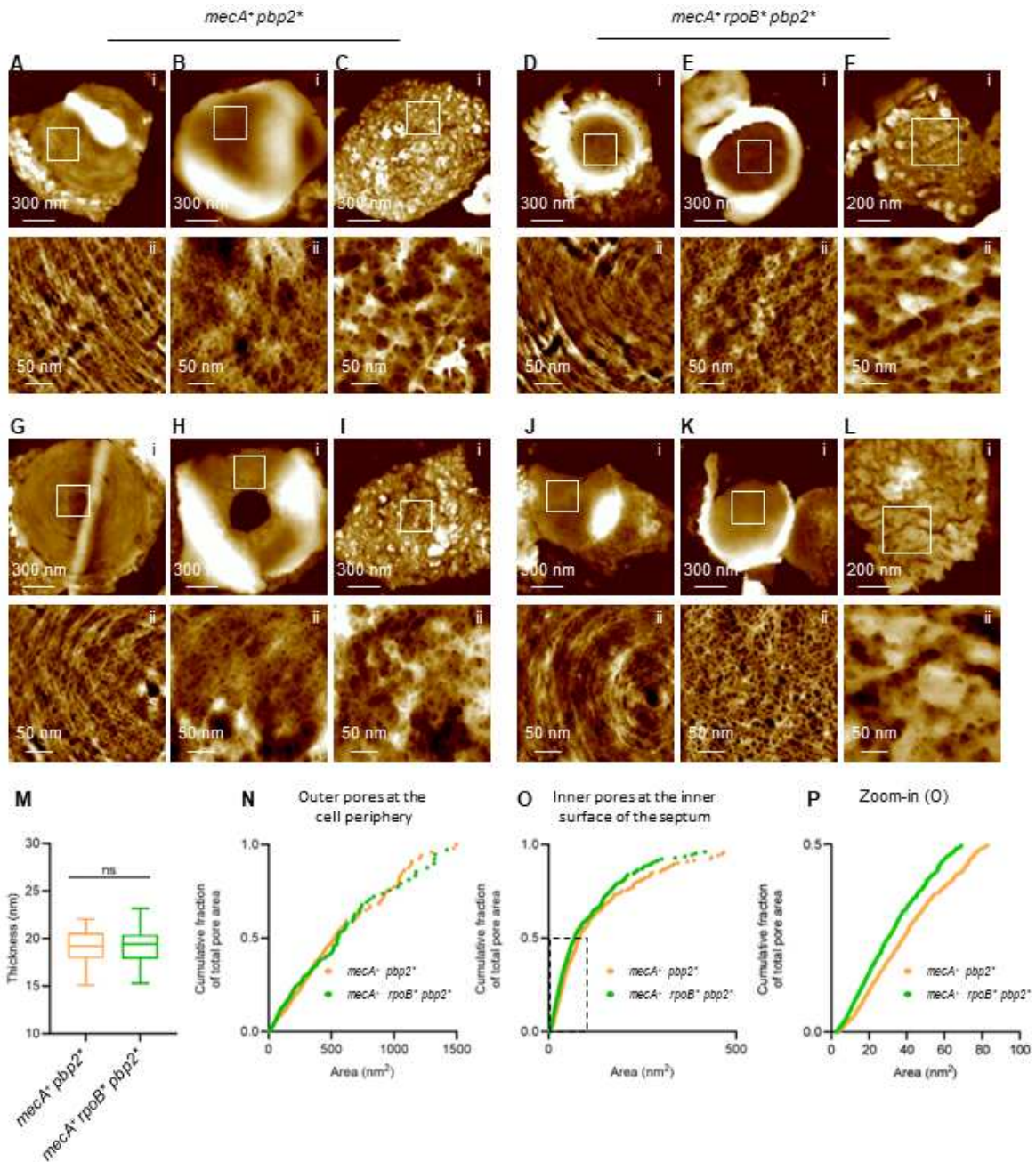


503

504 **Fig. S9.**

505 Role of PBP2 in cell morphology. (A-F) Fluorescence microscopy images of the SH1000
 506 derivatives *pbp2* (A), *mecA⁺ pbp2* (B), *rpoB^{*} pbp2* (C) and *mecA⁺ rpoB^{*} pbp2* (D) grown in

507 the presence (+ IPTG) or absence (- IPTG) of the inducer for 4 h. *mecA*⁺ *pbp2** (**E**) and *mecA*⁺
508 *rpoB** *pbp2** (**F**) were grown in the presence of IPTG at all times. All strains were incubated
509 for 5 min with ADA-DA clicked to Atto488 to show nascent PG, and counter labelled with
510 NHS-ester Alexa Fluor 555 to image the cell wall. Images are average intensity projections of
511 z stacks. Cells with dispersed, apparent ADA-DA incorporation (yellow arrowheads), no ADA-
512 DA incorporation (blue arrowheads) or mislocalized ADA-DA incorporation (white
513 arrowheads) are examples of cells that were classified as abnormal in panel **G**. (**G**)
514 Quantification of cellular phenotypes based on ADA-DA incorporation in **A-F**. From left to
515 right, *n* = 247, 235, 261, 288, 237, 273, 299, 309, 278 and 305. (**H**) Cell volumes of strains in
516 **A-F** measured by fluorescence microscopy after NHS-ester Alexa Fluor 555 labelling. Number
517 of cells analysed for each sample was *n* ≥ 300. Data are representative of three independent
518 biological experiments.



519

520 **Fig. S10.**

521 Surface-dependent nanoscale architecture of *mecA*⁺ *pbp2*^{*} and *mecA*⁺ *rpoB*^{*} *pbp2*^{*} revealed
 522 by AFM. AFM topographic images of the outer surface of the septum (A), the inner surface of
 523 the septum (B), and open mesh structure of the cell periphery (C) associated with the cell wall
 524 of *mecA*⁺ *pbp2*^{*}. (i) Low-resolution AFM images and (ii) corresponding higher-resolution
 525 images of the region indicated by the white boxes in (i). Topographical height (z) range for (i)
 526 are 100 nm, 330 nm, and 85 nm and for (ii) are 11 nm, 16 nm, and 45 nm respectively. (D-F)
 527 AFM images of the same cell wall locations for *mecA*⁺ *rpoB*^{*} *pbp2*^{*}; (i) and (ii) as above. The
 528 height scales for (i) are 200 nm, 140 nm, and 130 nm. The height scales for (ii) are 16 nm, 9
 529 nm, and 55 nm respectively. (G-I) AFM images of the PG structures associated with the
 530 following locations on the cell wall of *mecA*⁺ *pbp2*^{*}; (G) AFM images of the outer surface of
 531 the septum, (H) inner surface of an incomplete septum, and (I) open mesh structure of the cell

532 periphery; (i) and (ii) as above. Topographical heights (z) for (i) are 150 nm, 210 nm, and 85
533 nm. Topographical heights (z) for (ii) are 11 nm, 22 nm, and 51 nm respectively. **(J-L)** AFM
534 images of PG structures of the same locations in *mecA⁺ rpoB* pbp2**; (i) and (ii) as above.
535 Topographical heights (z) for (i) are 140 nm, 200 nm, and 130 nm and for (ii) are 12 nm, 14
536 nm, and 70 nm respectively. **(M)**, Plot of the measured thickness of dehydrated sacculi of
537 *mecA⁺ pbp2** and *mecA⁺ rpoB* pbp2** respectively. The number of independent fragments
538 measured for each strain was 20. Data were analysed using the Mann-Whitney non-parametric
539 statistical test (ns, not significant = 0.7180). **(N-O)** Cumulative fraction of total pore area as a
540 function of the area of the pores distributed across the open mesh surface of the cell wall
541 periphery surface **(N)** and the inner surface **(O)** of the septum of *mecA⁺ pbp2** and *mecA⁺*
542 *rpoB* pbp2**. **(P)** Zoomed-in plot of the region highlighted by the dashed box in **(O)**. Data are
543 representative of two independent biological repeats and five AFM independent images.

Strain	Oxacillin MIC ($\mu\text{g ml}^{-1}$)	Methicillin MIC ($\mu\text{g ml}^{-1}$)
SH1000 (SJF682)	≤ 0.25	0.5
<i>mecA</i> ⁺ (SJF4996)	2	4
<i>mecA</i> ⁺ <i>rpoB</i> * (SJF5003)	> 256	> 256
COL (SJF315)	> 256	> 256
Mu50 (SJF5041)	> 256	> 256
MRSA252 (SJF4821)	> 256	> 256
TW20 (SJF6101)	> 256	> 256
USA300 (SJF4703)	0.75	1-2
USA300 (HL) (SJF6109)	> 256	64-128
EMRSA 15 (SJF6025)	16-24	64
EMRSA15 (HL) (SJF6110)	> 256	> 256
<i>geh</i> :: <i>mecA</i> ⁺ (SJF5324)	4-8	-
<i>geh</i> :: <i>mecA</i> ⁺ <i>rpoB</i> * (SJF5323)	> 256	-
<i>mecA</i> ⁺ <i>lytH</i> (SJF5461)	12	-
<i>mecA</i> ⁺ <i>gdpP</i> (SJF5464)	≤ 2	-
<i>mecA</i> ⁺ <i>pde2</i> (SJF5460)	3	-
<i>mecA</i> ⁺ <i>rel</i> * (SJF5463)	> 256	-
<i>mecA</i> ⁺ <i>clpP</i> (SJF5459)	12-16	-
<i>mecA</i> ⁺ <i>clpX</i> (SJF5462)	6-8	-
<i>rpoB</i> * (SJF5010)	≤ 0.25	-
<i>lytH</i> (SJF5455)	≤ 0.5	-
<i>gdpP</i> (SJF5025)	≤ 0.5	-
<i>pde2</i> (SJF5454)	≤ 0.125	-
<i>rel</i> * (SJF5457)	≤ 0.5	-
<i>clpP</i> (SJF5453)	0.25	-
<i>clpX</i> (SJF5456)	0.25-0.38	-

545 **Table S1.**

546 Oxacillin and Methicillin MICs for *S. aureus* strains. The MICs for oxacillin and methicillin
547 were determined using E-test strips or the microdilution method (respectively) in triplicate as
548 described in Materials and Methods. -, Not determined.

Strain	Genotype and Markers	Source
<i>Escherichia coli</i>		
NEB5 α	<i>fhuA2 (argF-lacZ)U169 phoA glnV44 80 (lacZ)M15 gyrA96 recA1 relA1 endA1 thi-1 hsdR17</i>	New England Biolabs
<i>Staphylococcus aureus</i>		
SH1000	Functional <i>rsbU</i> ⁺ derivative of <i>S. aureus</i> 8325-4	(50)
COL	Healthcare acquired MRSA (HA-MRSA)	(51)
Mu50	HA-MRSA	(19)
MRSA252	HA-MRSA	(18)
TW20	HA-MRSA	(17)
USA300	Community-acquired MRSA (CA-MRSA)	(20)
USA300 (HL) (SJF6109)	High-level oxacillin resistant derivative of USA300	This study
EMRSA 15	CA-MRSA	(3)
EMRSA15 (HL) (SJF6110)	High-level oxacillin resistant derivative of EMRSA15	This study
VF17	SH1000 pGL485 (<i>lacI</i>); Cm ^R	(34)
RN4220	Restriction deficient transformation recipient	(52)

CYL316	RN4220 pCL112Δ19; Cm ^R	(53)
SJF4924	SH1000 <i>geh::Pspac-pbp2</i> , Kan ^R	This study
SJF5046	SH1000 <i>lysA::mecA rpoB^{H929Qkan}</i> ; Ery ^R , Kan ^R	(14)
<i>pbp1*</i> (SJF4656)	SH1000 <i>geh::Pspac-pbp1</i> <i>pbp1::pbp1* lacI</i> ; Tet ^R , Cm ^R	(8)
<i>pbp1* mecA⁺</i> (SJF5223)	SH1000 <i>geh::Pspac-pbp1</i> <i>pbp1::pbp1* lacI lysA::mecA</i> ; Tet ^R , Cm ^R , Ery ^R	(8)
<i>pbp1* rpoB*</i> (SJF5306)	SH1000 <i>geh::Pspac-pbp1</i> <i>pbp1::pbp1* lacI rpoB^{H929Qkan}</i> ; Tet ^R , Cm ^R , Kan ^R	This study
<i>pbp1* mecA⁺ rpoB*</i> (SJF5226)	SH1000 <i>geh::Pspac-pbp1</i> <i>pbp1::pbp1* lacI lysA::mecA</i> <i>rpoB^{H929Qkan}</i> ; Tet ^R , Cm ^R , Ery ^R , Kan ^R	(8)
Δ <i>pbp1</i> (SJF5106)	SH1000 <i>geh::Pspac-pbp1 Δpbp1 lacI</i> ; Tet ^R , Cm ^R	(8)
Δ <i>pbp1 mecA⁺</i> (SJF5224)	SH1000 <i>geh::Pspac-pbp1 Δpbp1 lacI</i> <i>lysA::mecA</i> ; Tet ^R , Cm ^R , Ery ^R	(8)
Δ <i>pbp1 rpoB*</i> (SJF5305)	SH1000 <i>geh::Pspac-pbp1 Δpbp1 lacI</i> <i>rpoB^{H929Qkan}</i> ; Tet ^R , Cm ^R , Kan ^R	This study
Δ <i>pbp1 mecA⁺ rpoB*</i> (SJF5227)	SH1000 <i>geh::Pspac-pbp1 Δpbp1 lacI</i> <i>lysA::mecA rpoB^{H929Qkan}</i> ; Tet ^R , Cm ^R , Ery ^R , Kan ^R	(8)
<i>pbp2</i> (SJF5630)	SH1000 <i>geh::Pspac-pbp2 pbp2::tet</i> <i>lacI</i> ; Tet ^R , Kan ^R , Cm ^R	This study

<i>mecA</i> ⁺ (SJF4996)	SH1000 <i>lysA::mecA</i> ; Ery ^R	(14)
<i>mecA</i> ⁺ <i>rpoB</i> [*] (SJF5003)	SH1000 <i>lysA-mecA rpoB</i> ^{H929Q} ; Ery ^R	(14)
<i>rpoB</i> [*] (SJF5010)	SH1000 <i>lysA::kan rpoB</i> ^{H929Q} ; Kan ^R ,	(14)
<i>mecA</i> ⁺ <i>pbp2</i> (SJF5663)	SH1000 <i>lysA::mecA geh::Pspac-pbp2 pbp2::tet lacI</i> ; Ery ^R , Kan ^R , Tet ^R , Cm ^R	This study
<i>mecA</i> ⁺ <i>rpoB</i> [*] <i>pbp2</i> (SJF5674)	SH1000 <i>lysA::mecA rpoB</i> ^{H929Q} <i>geh::Pspac-pbp2 pbp2::tet lacI</i> ; Ery ^R , Kan ^R , Tet ^R , Cm ^R	This study
GMSA015	SH1000 <i>lysA::ery</i> ; Ery ^R	(54)
<i>rpoB</i> [*] <i>pbp2</i> (SJF5690)	SH1000 <i>lysA::ery rpoB</i> ^{H929Q} <i>geh::Pspac-pbp2 pbp2::tet lacI</i> ; Ery ^R , Kan ^R , Tet ^R , Cm ^R	This study
<i>mecA</i> ⁺ <i>pbp2</i> [*] (SJF5807)	SH1000 <i>lysA::mecA geh::Pspac- pbp2* pbp2::tet lacI</i> ; Ery ^R , Kan ^R , Tet ^R , Cm ^R	This study
<i>mecA</i> ⁺ <i>rpoB</i> [*] <i>pbp2</i> [*] (SJF5809)	SH1000 <i>lysA::pmecA rpoB</i> ^{H929Q} <i>geh::Pspac-pbp2*(TP-) pbp2::tet lacI</i> ; Ery ^R , Kan ^R , Tet ^R , Cm ^R	This study
<i>geh::mecA</i> ⁺ <i>rpoB</i> [*] (SJF5323)	SH1000 <i>geh::mecA lysA::tet rpoB</i> ^{H929Q} ; Kan ^R , Tet ^R	(14)
<i>geh::mecA</i> ⁺ (SJF5324)	SH1000 <i>geh::mecA lysA::tet</i> ; Kan ^R , Tet ^R	(14)
NE1369	JE2 <i>lytH::Tn</i> ; Ery ^R	(55)
<i>lytH</i> (SJF5455)	SH1000 <i>lytH::Tn</i> ; Ery ^R	This study

<i>mecA</i> ⁺ <i>lytH</i> (SJF5461)	SH1000 <i>geh::mecA lysA::tet lytH::Tn</i> ; Kan ^R , Tet ^R , Ery ^R	This study
ANG1959	SEJ1 <i>gdpP::kan</i>	(56)
<i>gdpP</i> (SJF5025)	SH1000 <i>gdpP::kan</i>	This study
<i>mecA</i> ⁺ <i>gdpP</i> (SJF5464)	SH1000 <i>lysA::mecA gdpP::kan</i> ; Ery ^R Kan ^R ,	This study
NE1208	JE2 <i>pde2::Tn</i> ; Ery ^R	(55)
<i>pde2</i> (SJF5454)	SH1000 <i>pde2::Tn</i> ; Ery ^R	This study
<i>mecA</i> ⁺ <i>pde2</i> (SJF5460)	SH1000 <i>geh::mecA lysA::tet pde2::Tn</i> ; Kan ^R , Tet ^R , Ery ^R	This study
NE1714	JE2 <i>rel::Tn</i> ; Ery ^R	(55)
<i>rel</i> (SJF5457)	SH1000 <i>rel::Tn</i> ; Ery ^R	This study
<i>mecA</i> ⁺ <i>rel</i> (SJF5463)	SH1000 <i>geh::mecA lysA::tet rel::Tn</i> ; Kan ^R , Tet ^R , Ery ^R	This study
<i>pbp1</i> * <i>rel</i> (SJF5513)	SH1000 <i>geh::Pspac-pbp1</i> <i>pbp1::pbp1* lacI rel::Tn</i> ; Tet ^R , Cm ^R , Ery ^R	This study
<i>clpP</i> SJF5453)	SH1000 <i>clpP::Tn</i> ; Ery ^R	This study
<i>mecA</i> ⁺ <i>clpP</i> (SJF5459)	SH1000 <i>geh::mecA, clpP::Tn</i> ; Ery ^R Kan ^R	This study
<i>clpX</i> (SJF5456)	SH1000 <i>clpX::Tn</i> ; Ery ^R	This study
<i>mecA</i> ⁺ <i>clpX</i> (SJF5462)	SH1000 <i>geh::mecA, clpX::Tn</i> ; Ery ^R Kan ^R	This study

NE912	JE2 <i>clpP::Tn; Ery^R</i>	(55)
SJF1704	8325-4 <i>clpX::Tn; Ery^R</i>	Lab stock

550 **Table S2.**

551 Strains used in this study.

552 Cm^R – chloramphenicol, Ery^R – erythromycin, Kan^R – kanamycin, Tet^R – tetracycline

Name	Characteristics	Source
pCQ11-FtsZ-SNAP	pCQ11 derivative containing <i>ftsZ-snap</i> under Pspac; Amp ^R , Ery ^R	(57)
pGM074	pKASBAR-kan derivative with <i>ezaA-psmorange</i> ; Amp ^R , Tet ^R	(54)
pKB-Pspac- <i>pbp2</i>	pGM074 derivative containing Pspac, <i>S. aureus pbp2</i> RBS and full length <i>pbp2</i> ; Amp ^R , Kan ^R	This study
pKB-Pspac- <i>pbp2*</i>	pGM074 derivative containing Pspac, <i>S. aureus pbp2</i> RBS and full length <i>pbp2</i> with inactivated TP (<i>pbp2*</i>); Amp ^R , Kan ^R	This study
pMAD	<i>E. coli-S. aureus</i> shuttle vector with temperature-sensitive origin of replication in <i>S. aureus</i> and constitutively produced thermostable β -galactosidase encoded by <i>bgaB</i> ; Amp ^R , Ery ^R	(58)
pMAD- Δ <i>pbp2</i>	pMAD containing a deletion cassette for <i>S. aureus pbp2</i> ; Amp ^R , Ery ^R , Tet ^R	This study
pAISH1	TetR derivative of pMUTIN4; Amp ^R ; Tet ^R	(54)

553 **Table S3.**

554 Plasmids used in this study. Amp^R – ampicillin, Ery^R – erythromycin, Kan^R – kanamycin, Tet^R

555 – tetracycline

Name	Sequence 5'–3'
pCQ11-pbp2-F	agaaggagatatacatatggagtgaggaccgcgtatgac
pCQ11-pbp2-R	atttattatgcatttagaataggtagtgaatatacctgtaatccac
pKB-pbp2-R	cagctatgaccatgattacgttagtgaatatacctgtaatccac
pKB-Pspac-pbp1-F	ccttttttgcgccgggatccgcaaaaagttggtgactttatc
pbp2TP-F	ccctactggtggatctttaaacc
pbp2TP-R	tgaggatctgtgcttgg
pMAD- Δ pbp2-F	ccatggtaccgggagctcgacgatgaaaatacttttaataataaaatc
pbp2-up-R	acactatctgcaggtcatacgcggtcctcac
tetR-pbp2-F	gaccgcgtatgacctgcagatagtgtacgtaaaaag
tetR-pbp2-R	tatggtgagtgactctctcccaaagttgatc
pbp2-down-F	ctttgggagagagtccactcaacataaaatcctc
pMAD- Δ pbp2-R	ccatggtaccgggagctcgacgatgaaaatacttttaataataaaatc

556 **Table S4.**

557 Oligonucleotides used in this study.